UNIVERSIDADE DA BEIRA INTERIOR
Engenharia

Design of a Low Consumption Electric Car Prototype

Carlos Magno dos Reis Fonte

Dissertação para obtenção do Grau de Mestre em
Engenharia Aeronáutica
(Ciclo de estudos integrado)

Orientador: Prof. Doutor Miguel Ângelo Rodrigues Silvestre

Covilhã, outubro de 2015

"The phenomenon of turbulence was probably invented by the Devil on the seventh day of Creation (when the Good Lord wasn't looking)"

Peter Bradshaw

Dedicatória

Dedico esta dissertação de mestrado aos meus pais, Carlos Gonçalo Silva da Fonte e Elisabete do Céu Pires dos Reis Fonte e também à minha namorada Hilary Almeida Marques, por todo o apoio dado ao longo destes anos e por terem acreditado nas minhas capacidades. Esta dissertação é para vocês!

Agradecimentos

Quero agradecer o Professor Doutor Miguel Ângelo Rodrigues Silvestre, orientador desta dissertação, ao Professor Doutor José Carlos Páscoa Marques e ao Doutor Carlos Xisto a partilha do conhecimento e da ajuda valiosa para este projeto.

Também quero agradecer a todos os meus amigos, família e minha namorada pelo grande apoio dado e tempo dedicado. Muito Obrigado!

Resumo

Preocupados com o ambiente e a sustentabilidade, a Shell organizou nos últimos 30 anos uma competição de veículos de baixo consumo designada por Shell Eco-Marathon (SEM). O objetivo do veículo é atingir a velocidade média mínima de 25km/h, sendo o valor reduzido de arrasto um parâmetro importante para atingir um bom resultado. Ao longo dos anos as equipas da SEM usaram corpos fuselados parecidos com perfis alares e com uma baixa área frontal, contudo a presente equipa AERO@UBI decidiu criar um novo conceito para o desenho da carroçaria do veículo. Este corpo 3D também deriva de um perfil alar, usando uma transformação geométrica proposta por Galvão em 1968 em *"Nota técnica sobre corpos fuselados", São José dos Campos*, para a criação de corpos fuselados. De acordo com esse autor, é possível replicar a distribuição do coeficiente de pressão do perfil alar para o corpo 3D. Deste modo, mantêm-se as características de baixo arrasto do perfil alar. Através do uso do software CFD ANSYS Fluent fomos capazes de confirmar o conceito usado e examinar a aerodinâmica do veículo. Apesar do resultado não ter sido o ótimo, foi possível confirmar a teoria introduzida por Galvão. O veículo tem um comportamento similar ao do perfil com um $C_D \approx 0.088$ para uma área frontal de $0.3522m^2$. A análise dos resultados mostram que algumas modificações são necessárias para otimizar o veículo. Uma possível modificação é ajustar a transformação do perfil alar a fim de reduzir a acuidade do nariz para um melhor acordo entre o corpo 3D e a distribuição do coeficiente de pressão do perfil alar. Todavia, é possível com este conceito obter corpos de arrasto reduzido com uma transição da camada limite tardia, o que significa um consumo menor, tanto para aeronaves quanto para veículos terrestres.

Palavras-chave

Corpos Fuselados, Shell Eco-Marathon, CFD

Resumo Alargado

Preocupados com o ambiente e a sustentabilidade, a Shell organizou nos últimos 30 anos uma competição de veículos de baixo consumo designada por Shell Eco-Marathon (SEM). O objetivo do veículo é atingir a velocidade média mínima de 25km/h, sendo o valor reduzido de arrasto um parâmetro importante para atingir um bom resultado. Ao longo dos anos as equipas da SEM usaram corpos fuselados parecidos com perfis alares e com uma baixa área frontal, contudo a presente equipa AERO@UBI decidiu criar um novo conceito para o desenho da carroçaria do veículo. Este corpo 3D também deriva de um perfil alar, usando uma transformação geométrica proposta por Galvão em 1968 em *"Nota técnica sobre corpos fuselados", São José dos Campos*, para a criação de corpos fuselados. De acordo com esse autor, é possível replicar a distribuição do coeficiente de pressão do perfil alar para o corpo 3D. Deste modo, mantêm-se as características de baixo arrasto do perfil alar. O corpo 3D diz respeito a um corpo de revolução do perfil alar transformado. A partir desse corpo de revolução é aplicado o conceito de áreas equivalentes, sendo assim possível alterar as formas das secções transversais do corpo de revolução para uma melhor adaptação aos sistemas internos do veículo mantendo as características aerodinâmicas do perfil alar. O uso de um perfil alar conveniente é importante para este projeto, por isso foram impostos alguns critérios para a escolha do perfil, como uma grande extensão laminar e um baixo valor de arrasto. Através do uso do software CFD ANSYS Fluent fomos capazes de confirmar o conceito usado e examinar a aerodinâmica do veículo. Apesar do resultado não ter sido o ótimo, foi possível confirmar a teoria introduzida por Galvão. O veículo tem um comportamento similar ao do perfil com um $C_D \approx 0.088$ para uma área frontal de $0.3522 m^2$. A análise dos resultados mostram que algumas modificações são necessárias para otimizar o veículo. Uma possível modificação é ajustar a transformação do perfil alar a fim de reduzir a acuidade do nariz para um melhor acordo entre o corpo 3D e a distribuição do coeficiente de pressão do perfil alar. Todavia, é possível com este conceito obter corpos de arrasto reduzido com uma transição da camada limite tardia, o que significa um consumo menor, tanto para aeronaves quanto para veículos terrestres.

Abstract

Concerned with environment and sustainability, Shell has organized for the last 30 years a competition of energy efficient road vehicles called Shell Eco-Marathon (SEM). The vehicle is required to achieve a minimum mean cruise speed of 25km/h and a low drag value is an essential parameter to achieve a good result. Over the years SEM teams used a streamlined body similar to an airfoil with a minimized low frontal area, however AERO@UBI team decided to create a new concept vehicle body. This 3D body also derives from a 2D airfoil, but a geometric transformation introduced by Galvão in 1968 in *"Nota técnica sobre corpos fuselados", São José dos Campos*, for the creation of low drag fuselage is used. According to that author, it is possible to replicate the pressure coefficient distribution of the airfoil in the 3D body. Thus, maintaining the airfoil's low drag characteristics. Through the use of CFD software ANSYS Fluent it was possible to confirm the used concept and examine the vehicle aerodynamic. Although the final result was not optimal, it was possible to confirm the theory introduced by Galvão. The vehicle does have the same behavior as the airfoil with a $C_D \approx 0.088$ for a frontal area of 0.3522m^2. The results show that some modifications need to be made a future works to optimize the vehicle. One possible modification would be to adjust the airfoil transformation in order to decrease the sharpness of the vehicle's nose for a closer agreement between the 3D body and the airfoil's pressure coefficient distribution. Nevertheless, with this concept it is possible to design low drag bodies with late boundary layer transition which means a lower drag and energy consumption, both for airplanes and road vehicles.

Keywords

Low-drag body, Shell Eco-Marathon, CFD

Table of Contents

List of Figures

List of Tables

List of Abbreviations

SEM – Shell Eco-marathon

CFD – Computer Fluid Dynamics

DNS – Direct Numerical Simulations

LES – Large Eddy Simulation

RANS – Reynolds-Averaged Navier-Stokes

STL - Surface Tesselation Language

GUI - Graphical User Interface

List of Symbols

ρ_∞ - Fluid density $[kg/m^3]$

U_∞ – Fluid velocity $[m/s]$

S_{wet} – Wetted area (surface area) $[m^2]$

$S_{frontal}$ – Frontal area $[m^2]$

S_x – Frontal area of the component x

S – Frontal area of the vehicle

C_D – Drag coefficient

C_L – Lift coefficient

$C_{D,f}$ – Skin friction drag coefficient

$C_{D,P}$ – Pressure drag coefficient

$^x/_c$ – Dimensionless horizontal position of the airfoil

$^x/_l$ – Dimensionless horizontal position of the revolution body

$^r/_l$ – Dimensionless radius of the revolution body at position $^x/_l$

$^y/_c$ – Dimensionless vertical coordinate of the airfoil at position $^x/_c$

$r_{car}(x)$ – Section radius $[m]$

$A_{section}(x)$ – Transversal area of the section $[m^2]$

Re – Reynolds number

U_{car} - Vehicle velocity $[m/s]$

L – Vehicle length $[m]$

μ – Dynamic viscosity $[N \cdot s/m^2]$

y – Distance from the wall

ρ – Fluid density

μ - Viscosity

y^+ - Non-dimensional wall unit

u^+ - Non-dimensional velocity unit

τ_w – Wall shear stress

$maxX$,$maxY$ and $maxZ$ – maximum distance from the references plans for each axis

$minX$,$minY$ and $minZ$ – minimum distance from the references plans for each axis

n_x, n_y and n_z – number of elements for each axis

SCS – Surface Cell Size $[m]$

$BBCS$ – Bounding Box Cell Size $[m]$

RL – Refinement Level

$RFLT$ – Relative Final Layer Thickness

ΔE – Expansion Rate

n_{layer} – Number of Layers

Δs^* - First cell height

Chapter 1

1. Introduction

1.1 Introduction

The purpose of the present work was to design a vehicle body for a Shell Eco-Marathon (SEM) vehicle and study it through CFD simulation in order to evaluate its performance and possible improvements to the design concept.

The AERO@UBI is a battery electric prototype vehicle (**Error! Reference source not found.**) build by a team from Aeronautical Engineering of University of Beira Interior (UBI). AERO@UBI participated in the electric prototype category in SEM Europe 2014 and 2015 editions. On 2014 edition due to a technical issue in the motor controller it was impossible to achieve any results in the circuit. But, in 2015 with the controller problem fixed a 19th place was achieved with a consumption of 330.8 km/kWh.

Figure 1.1 - AERO@UBI vehicle at Eco-Shell Marathon Europe 2015 edition

Since the drag force value is an important parameter, it must be minimized to achieve a good result in SEM. With this in mind, a new concept of vehicle design was implemented herein for research.

In 1968, Aeronautical Engineer Francisco Leme Galvão introduced a concept where he explains that from a geometrical transformation of a 2D airfoil we can maintain similar aerodynamics

characteristics in a 3D body [1]. This concept was used to generate the present vehicle's body design. To evaluate it, Reynolds Averaged Navier Stokes (RANS) with turbulence model closure Computational Fluid Dynamics (CFD) simulations were performed with ANSYS Fluent software.

1.2 Shell Eco-Marathon Background

SEM is a racing competition dating back to 1939 when Shell Oil Company employees in USA made a bet over who could travel more kilometers with the same amount of fuel. In 1985, Shell revived the event starting the SEM annual competition. Since then, the competition expanded to two more continents, Europe and Asia. The teams compete in one of two possible categories: prototype and urban concept. These categories are split by energy type, internal combustion with various fuels, electric or hybrid propulsion. The prototype category has the objective of minimizing energy consumption despising the pilot comfort. The urban concept category focuses on practical designs. Regarding the energy type, internal combustion engine fuel types include: petrol; diesel; liquid fuel made from natural gas; ethanol and compressed natural gas, and electric propulsion can be powered by hydrogen fuel cells or lithium-based batteries.

Every year hundreds of teams show their vehicle concepts and test them on the track to achieve the highest range on the equivalent of one liter of fuel or one energy measuring unit, kWh in the case of the present battery electric vehicle. A good streamlined vehicle is important to decrease the drag force value, which is a critical parameter on prototype's concept, and thus achieve a good result. However the vehicle is constrain by some rules, from dimensions to safety, not impeding the creation of very low drag vehicles. One of the best examples of a prototype vehicle is the Pac Car II from ETH Zurich team (see Figure 2.13) beating the world record with a consumption of 5385km/l.

In 1999 the first team from UBI participated in SEM competition with the Maubere (Figure 1.2). In the year 2000 edition, a consumption of 371km/l was recorded. Twelve years later, in 2012, the same team but with an Urban Concept category vehicle won the first edition of a SEM similar competition, the Madrid Ecocity with 88km/l (Figure 1.3).

Figure 1.2 - Maubere from UBI team

For a prototype vehicle, since we have to decrease the drag force value, the solution found by most teams is to keep the frontal area in its minimum and create a streamlined body to prevent the flow separation such that the drag coefficient is kept as low as possible. Another design concept is to design the body with a curvature on the top in order to maintain the lift force value near zero. In the case of exterior wheels, the use of fairings can reduce the drag value but one has to be careful on fairings design because the wrong design can be prejudicial for the vehicle performance [2].

Figure 1.3 - UBIcar 2012 from UBI team

1.3 Objectives

The main objective of this project is to create a low drag vehicle for the AERO@UBI team SEM prototype vehicle while introducing a new concept of body shape creation and get all the information possible through RANS CFD simulation about the aerodynamics of the vehicle. It is also intended to verify the concept used for the first time in the creation of a road vehicle body, thus, introducing a new method of shape creation for low-drag vehicle bodies. To achieve this, the steps that have been followed during research were:

- The creation of the car body geometry and sizing with the intended new method;
- Analysis of the air flow around the vehicle, monitoring the aerodynamics performance parameters like drag, downforce and longitudinal pressure coefficient distribution;
- Compare the vehicle body performance with an initial equivalent body of revolution and the primitive airfoil;
- Analysis of the effects that ground clearance variation has on the vehicle aerodynamics;

- Analysis of the effects that angle of attack variation has on the vehicle;
- Based on the result of the different analyses, different variations of the vehicle shape are proposed for improvements.

1.4 Dissertation Structure

Following this introduction to the research topic, the next chapter presents a literature review covering the basic theory of road vehicle body design and adequate RANS CFD simulations and reports the state-of-art of SEM prototype vehicle body designs.

After the literature review, a chapter with an explanation of the methodology used throughout the study is given. The design concept and the drawing in CATIAV5 of the vehicle are explained in the first part. In the second part, the use of HELYX-OS for the mesh creation and the simulation settings of ANSYS Fluent software are described.

With the methodology explained, the results from the different simulations are presented and analyzed. From the analysis of the results, recommendations of improvements that could be implemented on the vehicle are presented.

Finally, a summary of conclusions and future works recommendations are listed in the last chapter.

1.5 Limitations and Dependencies

The main limitation of the present work was the available computational power. The mesh and simulations have been run on a laptop with a 2.5 GHz CPU formed by two cores with 8 Gb of RAM memory. Because of this limitation the mesh generation needed at last two days of iterations to create a mesh with an adequate quality and resolution. This limitation forced the mesh to have a poorer resolution than optimal, and the flow and vehicle geometry had to be simplified in order to reduce the mesh complexity and the cell number. A symmetry flow condition had to be applied to the vehicle symmetry plane, thus preventing the study of the flow sideslip angle on the body geometry design. The model is missing the wheels and respective cavities. This simplification changes the flow over the vehicle and the result of the simulations comparing to the actual vehicle flow. The drag generated by the real vehicle is, therefore, expected to be somewhat higher than the present results from the CFD simulations, but a prevision of the actual vehicle's drag is given based on a correction for the missing items according to the book Fluid-dynamic Drag by Sighard Hoerner [3].

Although, a significant loss of time was initially caused by attempts of creating meshes with successive better quality for the body geometry, at the end, all presented results have passed the necessary mesh refinement tests, therefore satisfying the aims of the project.

Chapter 2

2. Literature Review

In this Chapter the basic theory behind the design of the present vehicle is explained. The chapter is split into three sections. The first thus covering the basics of road vehicle aerodynamics and the different parameters that affect the vehicle performance. Second, CFD simulation is covered and finally state-of-art of SEM vehicles is reviewed.

As we can see in Figure 2.1, the aerodynamic force can be considered as three distinct forces. These force are separated by 90 degrees, creating a Cartesian coordinate system. On the Z axis we have the vertical force named lift, on the X axis we have the horizontal force named drag, and on the Y axis we have the lateral force named side force. In our case we will focus on the lift and drag forces only.

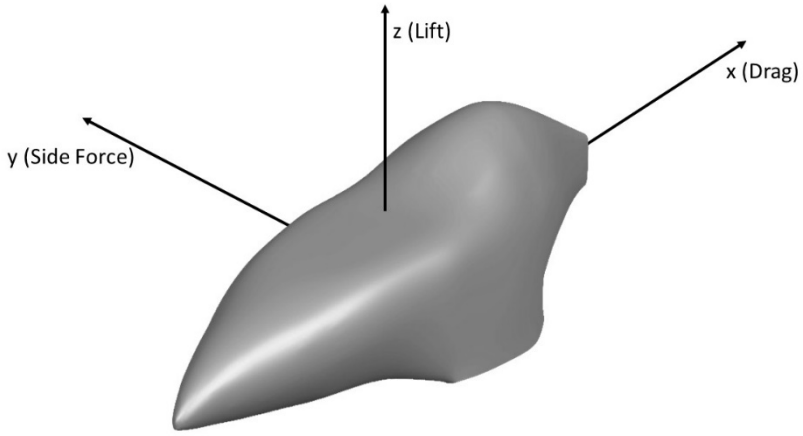

Figure 2.1 - 3D axis system to define aerodynamics forces

In this road vehicle design context, in general, the vertical force will affect the vehicle on the opposite way of lift, which is, pushing the car towards the ground. Hence the value of the lift force will be negative. The correct term used to describe this force is downforce, which is the positive force towards the ground.

2.1 Basic Vehicle Body Design Parameters

The basics of the aerodynamics of a road vehicle are described on multiple theory books. For our case we will describe three important parameters that have a big impact on the vehicle's aerodynamic performance. These are the ground clearance, the angle of attack of the body and its frontal area. All of these parameters depend mostly on the vehicle body shape.

2.1.1 Ground Clearance

Ground clearance can be described by the shortest distance between the flat road and vehicle body. In aerodynamics the ground clearance is one of the parameters affecting for the ground effect and so the downforce magnitude and the vehicle drag.

As we can see in Figure 2.2, downforce increases if ground clearance is reduced. That can be explained by the Bernoulli's equation [4]. If the cross-section area of the gap between the body and the ground is reduced, the speed of the air flow must increase, thus generating a lower static pressure. The decrease of pressure will produce a suction effect directed to the ground, thus generating more downforce. This effect is called ground effect.

It's also possible to see that a region exists where the ground clearance drops below h/L = 0.025. Here, the value of downforce decreases abruptly. This happens because at this non-dimensional distance the effects of viscosity start to be dominant, thereby "blocking" the flow under the body.

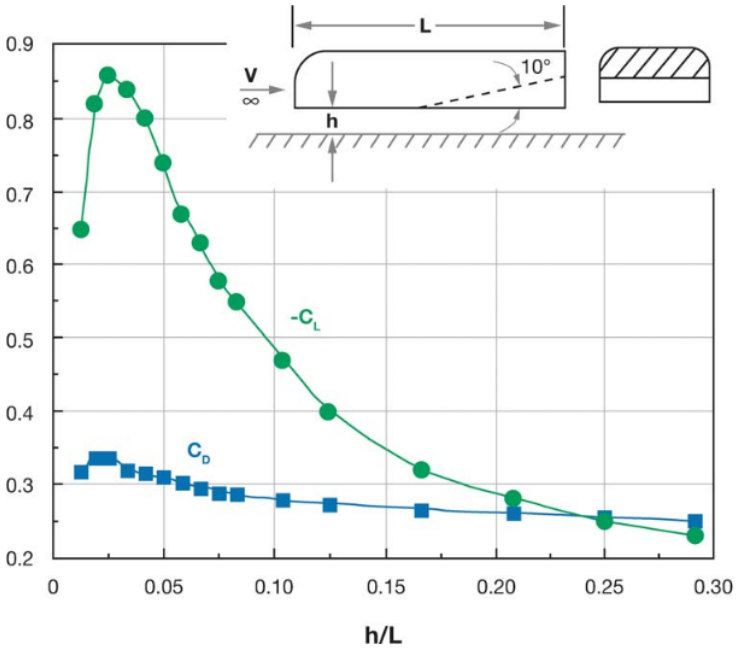

Figure 2.2 - Lift and drag coefficient variation with ground clearance [5]

Tamai explains in [6] that the drag of a moving vehicle as the same behavior as the Figure 2.3, where it is possible to see an optimal value of ground clearance regarding the minimization of drag. Tamai also suggest to set the minimal ground clearance between 0.15m and 0.25m for torpedo-shaped bodies.

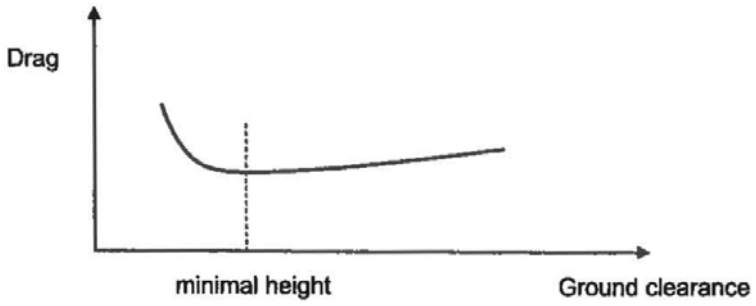

Figure 2.3 - Minimal ground clearance [6]

2.1.2 Body Angle of Attack

The angle of attack is defined by the angle between the freestream (parallel to flight path) and the mean cord of an airfoil (see Figure 2.4). In aerodynamics the lift changes with the angle of attack and, generally, the greater the angle of attack, the greater the lift. For an airfoil if we have an excessive angle of attack, the flow separates the upper surface with a loss of lift that is denominated stall [4].

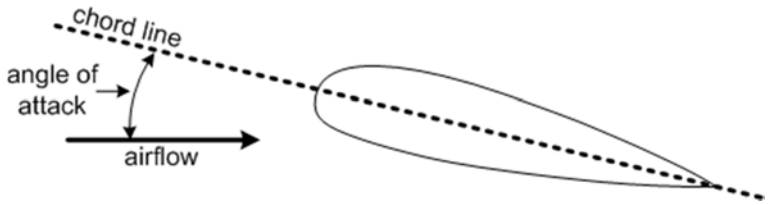

Figure 2.4 - Representation of angle of attack for an airfoil

The angle of attack of the body has a strong aerodynamic influence also in road vehicles like Katz [7] explains. In this case, the angle of attack is defined as the angle between the road and the vehicle's x axis. The change of attitude on a vehicle is similar to a wing, that is, the lift increase when the angle of attack increases as it can be seen on Figure 2.5. For a smooth underbody vehicle the lift slope can be very large. The drag coefficient has a minor change when the angle of attack is changed, mainly due to a variation in the boundary layer thickness.

In can be that the body incidence is an important parameter to take into account when designing the present SEM vehicle body. The shape of SEM vehicles in prototype category is typically very similar to a free falling drop, that's why it's important to consider the angle of attack to avoid an excessive value of downforce since the later would add normal force to the wheels rolling friction force.

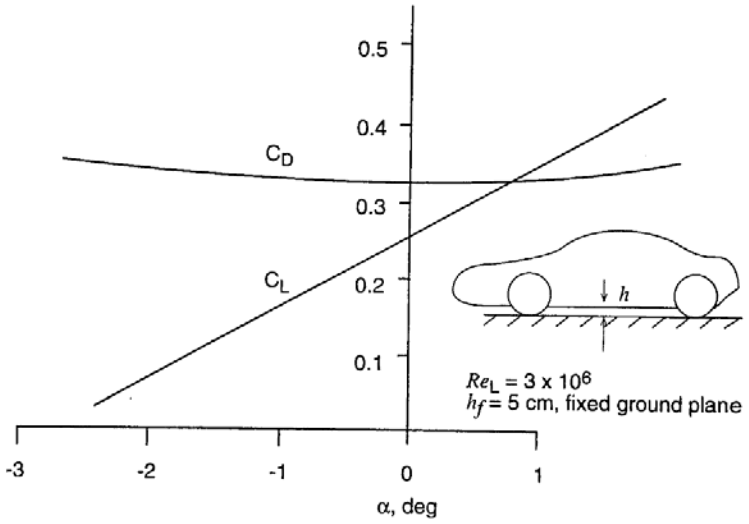

Figure 2.5 - Lift and drag coefficient versus angle of attack for a generic sedan [7]

2.1.3 Frontal Body Area and Wetted Area

On a body moving through fluid, two distinct forces will be present throughout, one tangent to surface, τ (wall shear stress) and one perpendicular to the surface, p (pressure) as it can be seen in Figure 2.6.

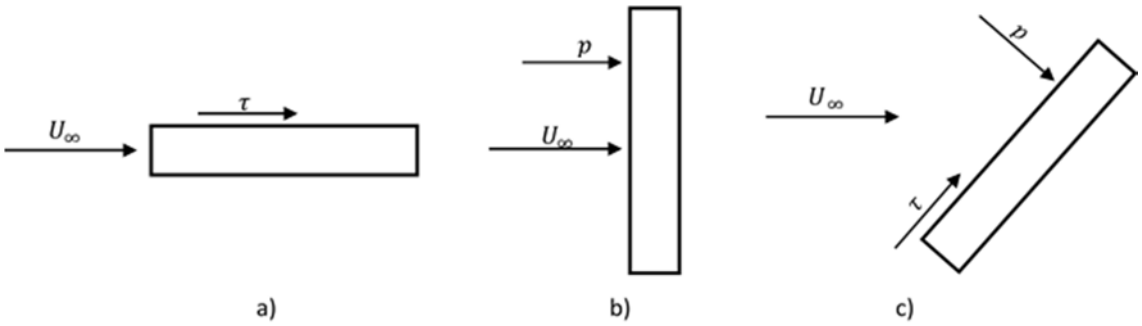

Figure 2.6 - Illustration of forces produced by the fluid. a) Tangential force. b) Perpendicular force. c) Mixed forces.

The integral of the tangential force on the body surface is called skin friction drag, D_f, and the perpendicular force is called pressure drag, D_P. The combination of this two type of drag form the total parasite drag, and they can be defined by:

$$D_f = \frac{1}{2}\rho_\infty U_\infty^2 S_{wet} C_{D,f} \tag{2.1}$$

$$D_P = \frac{1}{2}\rho_\infty U_\infty^2 S_{frontal} C_{D,P} \tag{2.2}$$

where:

ρ_∞ - Fluid density $[kg/m^3]$

U_∞ – Fluid velocity $[m/s]$

S_{wet} – Wetted area (surface area) $[m^2]$

$S_{frontal}$ – Frontal area $[m^2]$

$C_{D,f}$ – Mean skin friction coefficient

$C_{D,P}$ – Pressure drop drag coefficient

Analyzing the both equation it can be seen that the major factor to the variation of drag is the area. When the area increases, the drag increases also. Although these two drag react with different type of area definitions:

- Frictional drag depend on wetted area, area in contact with fluid flow, (see Figure 2.7b).
- Pressure drag depends mostly on frontal area[1], area projected on a plane normal to the flow (see Figure 2.7a).

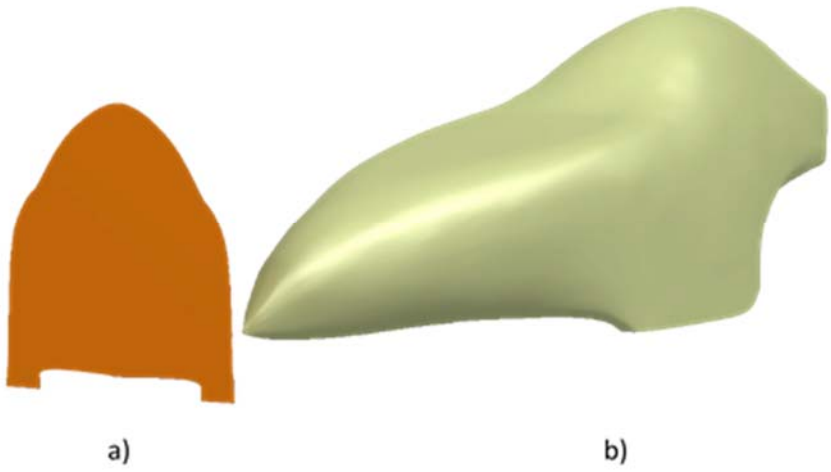

Figure 2.7 - Representation of a) Frontal area and b) Wet area

One can conclude that if we want to minimize the frictional drag we have to decrease wet area, on the other hand, if we want to minimize the pressure drag we have to decrease the frontal area. If no significant separation occurs, the frictional drag prevails, thus the main interest should be to minimize the wetted area.

2.1.4 Basic Aerodynamic Shapes

Basic shapes for vehicles that can create downforce with a minimum drag force are presented herein. Some of the possible shapes are shown in Figure 2.8.

[1] In fact pressure drag increases with friction drag

The first shape configuration, Figure 2.8A, is aimed to reach a very low drag value, and is usually applied to speed-record vehicles that run along straightaways. With that configuration it is possible to change the value of downforce by adjusting the incidence/angle of attack of the vehicle. For high-speed turning vehicles, the best configuration is the inverted wing, Figure 2.8B, because of the ground effect produced by the wing and the low value of drag.

The "catamaran" concept, Figure 2.8C, is the shape usually used in prototype race vehicles. With the wheels covered by the two sides of the vehicle, it results in a shape with a central tunnel ending with a rear slope, making the under vehicle a venturi tube. Since the free stream is ducted under the vehicle, the area of flow separation is reduced on the back of the vehicle, creating an ideal high-downforce and low-drag configuration.

SEM vehicles use a concept similar to "catamaran", but instead of the vehicle be covered on the two sides, only the wheels are covered, with the use of fairings. Reducing the effect of downforce and have a low-drag body.

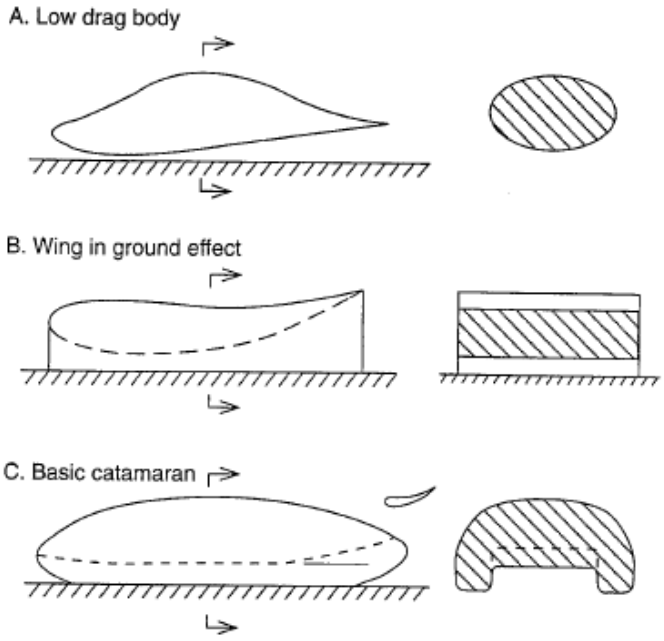

Figure 2.8 - Basics conceptual shapes (Adapted from [7])

2.2 CFD Simulations of Road Vehicle Aerodynamics

Computational Fluid Dynamics (CFD) simulations are based on solving the equations of conservation that model fluid flows. One of the advantages of CFD simulations is that it is more affordable than an experiment in a wind tunnel. It is possible to realize a parametric study with a substantial reduction of lead time, study complex system under hazardous conditions with a great level of detail of results and work in large volume system impossible to conduct in an experiment [8].

CFD codes are structured around numerical algorithms that can tackle fluid flow problems. This structure is divided in three main elements, which are, a pre-processor, a solver and a post-processor [8].

2.2.1 Pre-processing

Pre-processing consists of the input of a flow problem to a CFD program and it can be divided in the following stages:

- Definition of the geometry of the region of interest - domain;
- Grid generation, which is, the division of the domain in small elements;
- Selection of the physical phenomena that need to be modelled;
- Definition of fluid properties;
- Specification of appropriate boundary conditions.

The accuracy of a CFD solution is proportional to the number of elements (cells) in the grid, and generally for a larger number of cells the better is the solution. However it is important to see the relation between the accuracy of a solution and its cost in terms of necessary computer hardware and calculation time. For that reason it's necessary to study the mesh independency of the solution to reach an optimal mesh with enough accuracy and minimal computational resources.

Is also important to select a good model depending on the physical phenomena. In the case of turbulence modelling we want to have a good and complete description of the turbulent flow, however an analytical solution doesn't exist even for the simplest turbulent flow. As it is known a turbulent flow is known as a function of space and time, and it can only be obtained by solving the Navier-Stokes equations [9].

To solve the problem of turbulence simulation some solutions exist, like Direct Numerical Simulations (DNS), Reynolds-Averaged Navier-Stokes (RANS) and Large Eddy[2] Simulation (LES).

Direct Numerical Simulations (DNS) - The DNS is the most accurate simulation, since all the spatial and temporal scales of the flow are resolved by the time-dependent Navier-Stokes equations without any simplifying assumption.
Large Eddy Simulation (LES) - The turbulent flow is characterized by eddies with a wide range of length and time scales where:

[2] Eddy – Is the swirling of a fluid when the fluid flows past an obstacle, thus creating a reverse current behind the obstacle.

- The largest eddies are compared to the characteristic length of the mean flow;
- The smallest scale are responsible for the dissipation of turbulence kinetic energy.

Reynolds-Averaged Navier-Stokes (RANS) – RANS simulation is a simplest version of DNS, where the Navier-Stokes equations are resolved by the mean time simplified form and fluctuating components, like velocity and pressure [10]. Nevertheless, closure equations know as turbulence models are needed.

2.2.2 Solving

To obtain the numerical solution there are three distinct techniques: finite difference, finite element and spectral methods. The main differences between these three methods are associated with the way in which the flow variables are approximated and with the discretization processes. We can find more information about these method in reference [8].

In the overall, the solver is to perform the following steps:

- Approximation of the unknown flow variables values for each cell by means of simple functions of the neighboring cells;
- Discretization by substitution of the approximations into the governing flow equations and subsequent mathematical manipulations;
- Solution of the algebraic equations.

2.2.3 Post-processing

The post-processing consists in analyzing the obtained solution obtained. For that, CFD packages are equipped with versatile data visualization tools. These include:

- Domain geometry and grid display;
- Vector plots;
- Line and shaded contour plots;
- 2D and 3D surface plots;
- Particle tracking;
- View manipulations (translation, rotation, scaling, etc.);
- Color postscript output.

2.2.4 Blockage Effect

Like the wind-tunnel tests, in CFD simulations one has to be aware of some effects that can lead to errors in the solution. One of these effects is the blockage effect [11]. In a CFD simulation or wind-tunnel test there is a control volume/test chamber with a determined cross section area perpendicular to the flow. In this test section, the flow is partially blocked by the

body. When the walls of the control volume are far away from the body, the streamlines around the body are not affected by the walls (see Figure 2.9a), but if these walls are too close to the body, they will cause the flow to move faster in the gap between the model and the walls (see Figure 2.9b), creating errors on drag and lift readings [7].

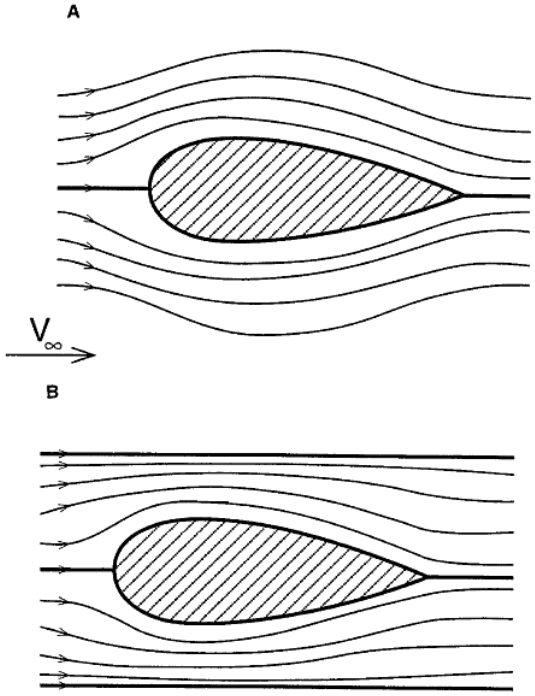

Figure 2.9 - Blockage effect illustration a) Wide away walls b) too-close walls [7]

In order to avoid the flow distortion due to this effect, a measure parameter called blockage ratio is used. The ratio is defined in Equation (2.3), and it's the frontal area of the body (blockage area) over the test section area of the control volume [12].

$$Blockage\ ratio = \frac{Body\ frontal\ area}{Control\ Volume\ sectional\ area} \tag{2.3}$$

To optimal situation is a very low blockage ratio, but we have to take in account that a big control volume can be prejudicial due to the computational cost and time that involves or due to the size of the wind-tunnel/test model. In conclusion, the control volume for the present vehicle CFD simulations has to be big enough to avoid the blockage effect, but also small enough to avoid an excessive number of cells and computational resources. In [13] it is recommended to maintain the blockage ratio under 7.5% for good results.

2.2.5 Boundary Layers Simulation

The fluid in motion close the surface of the vehicle will adhere to it, that phenomenon is due to the frictional force that retards the motion of the fluid in a thin layer near the wall. In that layer the velocity near the wall, with the no slip condition, is zero and it increases to its full

value which corresponds to external frictionless flow. This layer is called the boundary layer [14] (see Figure 2.10).

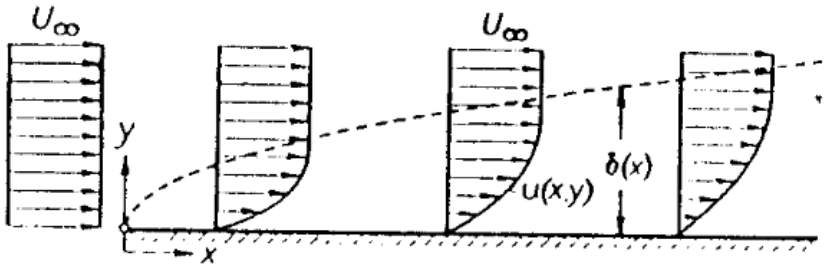

Figure 2.10 - Sketch of boundary layer on a flat plate in parallel flow at zero incidence [14]

In a first stage of the boundary layer the flow is laminar, but after the flow has reached a certain distance after the leading edge, the boundary layer becomes turbulent. The transition to turbulence is strongly affected by factors such as pressure gradient, disturbance levels, wall roughness and heat transfer [8]. Due to the viscous effect near the wall, the turbulent boundary layer has more friction on the surface then the laminar, thus causing an increase in drag.

In terms of turbulent boundary layer it is appropriate to describe it using a non-dimensional wall unit y^+, and velocity u^+ defined as:

$$u^+ = \frac{U}{u_\tau} = f\left(\frac{\rho u_\tau y}{\mu}\right) = f(y^+) \tag{2.4}$$

where,

y – Distance from the wall μ - Viscosity

ρ – Fluid density

Equation (2.4) is called the law of the wall [8]. Where u_τ is the friction velocity and is defined as:

$$u_\tau = \sqrt{\frac{\tau_w}{\rho}} \tag{2.5}$$

where,

τ_w – Wall shear stress

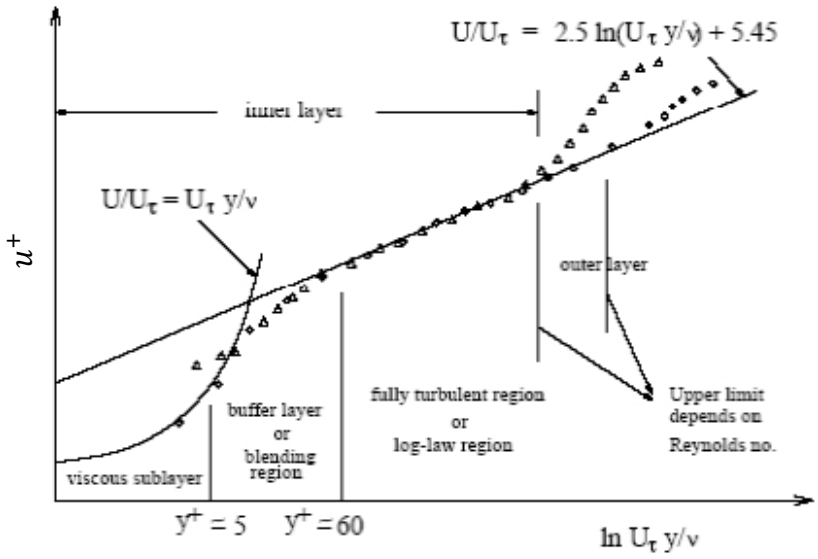

Figure 2.11 – Near wall region turbulent flow subdivision (Adapted from [15])

In Figure 2.11, four regions are highlighted in turbulent flow near the surface:

- **Viscous sublayer** – Near the wall, where the turbulent shear stress is absent the fluid becomes stationary and is dominated by viscous shear. In practice this layer is very thin ($y^+ < 5$) and it is possible to assume that the shear stress is constant and equal to the wall shear stress. Since the flow in this layer is approximately laminar, the following assumption can be made for the viscous sublayer [8]:

$$u^+ = y^+ \tag{2.6}$$

- **Buffer layer** – The region outside the viscous sublayer ($5 < y^+ < 60$) is called the buffer layer. In this region the viscous and turbulent stresses are approximately equal [16].
- **Log-Law layer** – After the buffer layer ($60 < y^+ < 500$) lies the log-law layer. In this region viscous and turbulence effects are also predominant. The shear stress τ is assumed to be constant and equal to the wall shear stress. With that it is possible to relate u^+ and y^+ [8]:

$$u^+ = \frac{1}{\kappa}\ln y^+ + B = \frac{1}{\kappa}\ln(Ey^+) \tag{2.7}$$

  Equation (2.7) is called the log-law and κ, B and E are universal constants valid for all turbulent flows. For a smooth walls $\kappa = 0.4$ and $B = 5.5$ (or $E = 9.8$), wall roughness causes a decrease in the value of B.
- **Outer layer** – The outer layer ($y^+ > 500$) is region far from the wall where the flow is dominated by inertia and free from direct viscous effects. In this region the velocity and distance are related by [8]:

$$\frac{U_{max} - U}{u_\tau} = \frac{1}{\kappa}\ln\frac{y}{\delta} + A \qquad (2.8)$$

where A is a constant.

Equation (2.8) represents the logarithmic form of the overlap region where the log-law and velocity-defect law (or law of the wake) become equal.

In a general form, the viscous sublayer, buffer layer and log-law layer can be joined forming the inner region, and the outer layer formed by the outer region. The inner region correspond 10% to 20% of the total thickness of the wall layer [8]. With this information is deduced that the mesh resolution near the wall must be good in order to have an accurate solution of the turbulence equations within the boundary layer.

2.2.6 Verification and Validation of CFD Simulations

In order to achieve a certain level of credibility of CFD simulations some procedures have to be realized. The American Institute of Aeronautics and Astronautics (AIAA) presented in 1998 a guide for the verification and validation of CFD simulations [17]. It explains that to assess credibility of simulations a verification has to be carried out. Verification is the process of determining if a CFD simulation accurately represents the conceptual model and validation is the process of determining if the CFD simulation represent the real world phenomena. In other words, verifications determine if the problem has been properly solved, and validation determines if the correct problem has been solved.

The verification process can be done on CFD software by accessing a multitude of variables such as the mass flow rate conservation, and the residuals convergence. Validation can be realized with the use of benchmark experimental data. For the automobile industry the most common benchmark case in use is the Ahmed body [18] (see Figure 2.12).

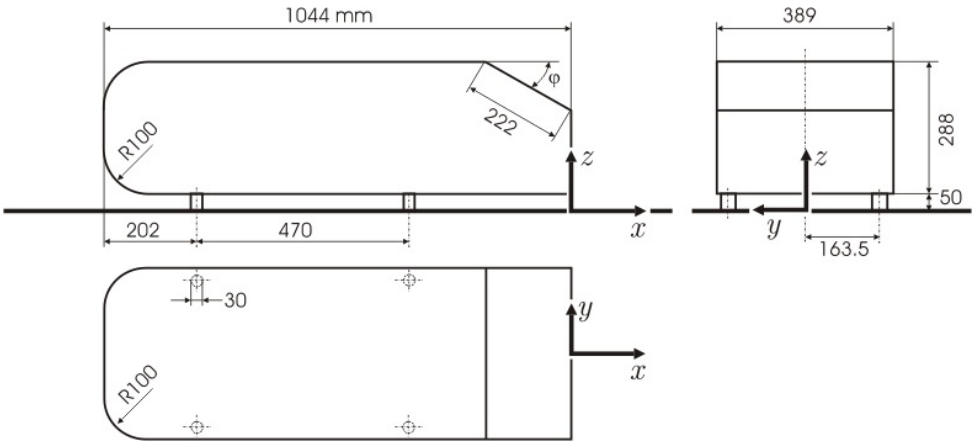

Figure 2.12 - Dimensions of Ahmed Body

2.3 SEM Vehicle Aerodynamics – State of the Art

In this section we will evaluate the current SEM aerodynamics. However there is not a lot of public information available about SEM vehicles

The first vehicle to be analyzed is the Pac Car II (see Figure 2.13) from ETH Zurich team who participated in the prototype-hydrogen class, winning the 2005 edition of SEM Europe. In reference [19] the authors explain that one has to take in account design constraints such as: race regulations; ergonomics and aerodynamics.. The preliminary design of Pac Car II was based on airfoils on the top and side views, natural laminar flow airfoils were used. Based on wind tunnel trials and CFD analysis the authors discovered that the wheels fairing design has a great impact on the aerodynamic quality. The use of slender wheel fairings reduced the frontal area and decreased the trailing-edge angle, generating a lower pressure gradient along the body vehicle and eliminating separated flow regions. The front wheels camber was also a relevant factor to reduce the drag value through a smaller frontal area, in Pac Car II they were tilted 8º. All these design concepts led to a vehicle with a frontal area of $0.254m^2$ and a value of drag coefficient of 0.07, and it can be seen in Figure 2.13, the side view profile of the vehicle was cambered to achieve a zero-lift, so reducing the drag value.

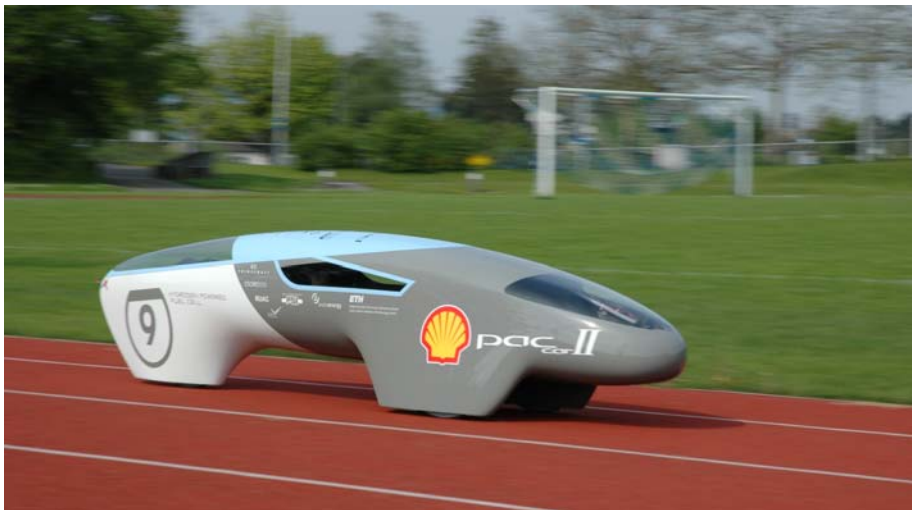

Figure 2.13 - Pac Car II from ETH Zurich team [20]

In 2009 edition of SEM Europe, XTEAM from Politecnico di Milano went with the ARTEMIDe (see Figure 2.14), despite the fifth place on prototype-hydrogen class the team won the "Autodesk Design Award" for the quality of the project, the choice of materials and the solution adopted for safety and maintenance [21]. One of the main goal of the team was the reduction of motion frictions. For that they designed a clean design profile. They covered the wheels with fairings. The rear wheel had connected the steering and propulsion system. The body also had a curvature on the top to reduce the effect of downforce. The final vehicle specifications are a frontal area of $0.284m^2$ and a drag coefficient of 0.1 [22].

Figure 2.14 - ARTEMIDe from XTEAM [21]

The team H2politO from Politecnico di Torino presented in 2012 edition of SEM Europe the IDRApegasus (see Figure 2.15), reaching the third place in prototype-hydrogen class. Like they explain in [23] their goal was to obtain the lowest drag, taking into account the constraints of race regulations, ergonomics and aerodynamics. To achieve a low product of frontal area time drag coefficient, some concept solutions were implemented: as it can be seen in Figure 2.15, they integrated the wheels inside the vehicle body and added a camber of 8° to the front wheels, the steering is made by the rear wheel where the propulsion system is mounted. All these concepts were similar to the PAC CARII, but they obtained a frontal area of 0.258m^2 for a drag coefficient of 0.093.

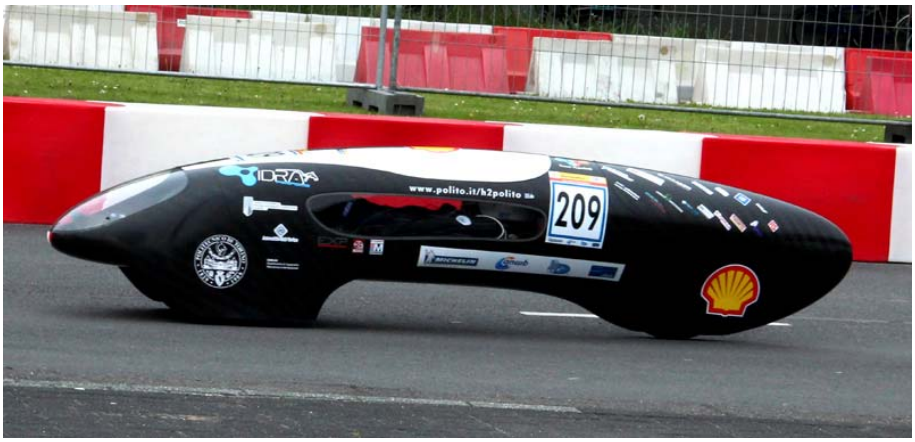

Figure 2.15 - IDRApegasus from H2politO team [24]

With 21 victories on the annual event, Microjoule from La Joliverie team is *"the team to beat in the Prototype petrol category"* [25] (see Figure 2.16). In 2009 they won the SEM 2009 Europe edition, with a consumption of 37771km/l. The vehicle as a body shape similar to a water droplet, with the wheels completely embedded on the bodywork. This concept reduces the

ground clearance to the most and provides a low frontal area, approximately 0.31m^2. It is also possible to see that the top has a small curvature to reduce the downforce effect, achieving a drag coefficient of 0.1 [26].

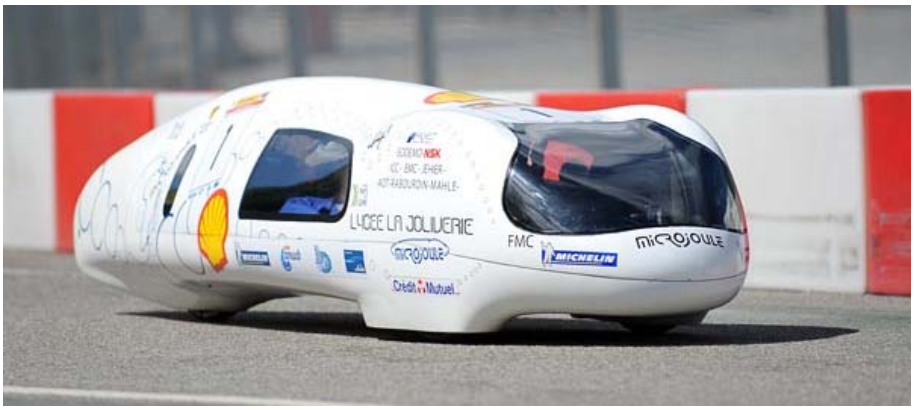

Figure 2.16 - Microjoule from La Joliverie team

Another good reference is the Fancy Carol prototype fuel vehicle, from Japan (see Figure 2.17). With a totally different vehicle body shape, the Fancy Carol won in 2004 a world record during a SEM United Kingdom event, with a consumption of 3963km/l [27]. This vehicle adopted a constant ground clearance all over the under body to reduce the suction effect and so the downforce. The wheels are also totally covered reducing the drag area by 12%. Another particularity is the minimization of the vehicle's size and frontal area, which are important to reduce the drag value. These concepts leads to a vehicle with a frontal area of 0.21m^2 and a drag coefficient of 0.12 at 70km/h [2].

Figure 2.17 - Fancy Carol from Japan

Despite of the lack of specific literature covering SEM vehicles aerodynamics, it was possible to deduce some important factors common on prototype vehicles that have a huge impact on vehicle performance. These factors must be taken in account when designing a prototype vehicle. The most important factors are the following ones:

- Low frontal area;
- Top body curvature (reducing downforce and so reduce drag coefficient);
- Laminar flow extension;
- Wheels fairing;
- Body angle of attack.

Chapter 3

3. Methodology

This chapter describes the process of AERO@UBI vehicle body design, the mesh generation process and the solution options used for the simulations. Therefore, initially this chapter will present the concept used to create the body geometry, the process of design in CATIA V5R20 and an improvement of the first design, later performed in Blender 2.73. In this chapter it is also introduced the use of the XFLR5 software in the process. In a second section, the CDF mesh generation with HELYX-OS software on Ubuntu is presented, followed by the explanation on the use of ANSYS Fluent as the solver.

3.1 Aerodynamic Design of the Vehicle

3.1.1 Design Concepts

Like the other SEM vehicles in competition, the principal objective on the design of the body is the minimization of the drag force. For that, it exists a wide range of solution concepts from the minimization of the frontal area to the use of certain body shapes, like those presented in Chapter 2.

From a long time ago that the dolphins and whales are subjects of aerodynamic studies. There are many references that describe the dolphins' bodies as being related to modern low drag laminar flow airfoils [28] [29]. There are also studies to recreate the whales' fins planforms for airplane wings. Galvão [1] wrote a paper about the similarity of the shark body shapes and airfoils. He discovered that their body is like a laminar flow symmetric airfoil with its thickness altered to exaggerate the airfoil section shape and he gave mathematic proof. With that he proposed a relation between a 2D airfoil and a 3D revolution body that will have the same pressure coefficient distribution along the longitudinal axis. In this way it is possible to minimize the drag of a fuselage using widely available airfoil data. The relation he came up with can be characterized by the equation (3.1). In Figure 3.1 it can be seen the visual representation of the application of the equation for the symmetric airfoil NACA 0012.

$$100 \cdot \frac{r}{l} = \left(100 \cdot \frac{y}{c}\right)^{3/2} \tag{3.1}$$

where,

x/c – Dimensionless horizontal position of the airfoil

x/l – Dimensionless horizontal position of the revolution body

r/l – Dimensionless radius of the revolution body at position x/l

y/c – Dimensionless vertical coordinate of the airfoil at position x/c

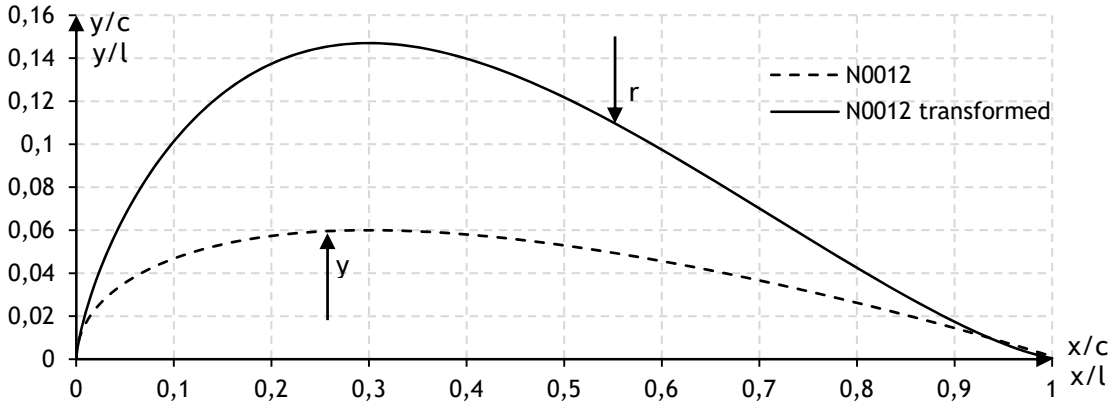

Figure 3.1 - NACA 0012 transformation by equation (3.1)

A second concept was introduced for the vehicle body design, the equivalent body of revolution. This concept is based on the transonic equivalence rule, which states that the flow far away from a slender body becomes axisymmetric and equal to the flow around an equivalent equal cross-sectional area body of revolution [30]. This concept will allow the new body have the same pressure coefficient distribution along the longitudinal axis as the body of revolution created by the transformed airfoil. With these two concepts it was possible to create a procedure for the creation of the present vehicle body:

1. An initial vehicle design mainly based on ergonomics to evaluate the internal volume needed for the pilot and other systems;
2. Analyze the radius distribution of the first body considering the equivalent body of revolution concept;
3. Select an appropriate airfoil;
4. Apply the geometric transformation (3.1) to the created airfoil;
5. Check if the transformed airfoil satisfies the required internal volume radius distribution;
6. Divide the body of revolution in sections along the longitudinal axis;
7. Adapt each section shape along the longitudinal axis according to internal volume necessity, in the corresponding longitudinal position, keeping the same section area value to satisfy the equivalent body of revolution concept.

In sum, the design consists in the replication of the pressure coefficient distribution of an airfoil with late boundary layer transition point to have a lower drag. With the transformation applied to the airfoil, it is created a 3D body of revolution. From the later, comes the creation of the new body adapted to the internal volume shape, but respecting each equivalent section area of the body of revolution.

Figure 3.2 - Flowchart of implemented concept

3.1.1.1 Concept evaluation

The first equation determined by Galvão [1] is shown on equation (3.2). As it can be seen the only difference is the value of the exponent, increasing from 1.17 to 1.5. Galvão [1] explained that this change is due to have a better approximation of the velocity gradient. This change rises a question though, what is the effect on pressure distribution on the 3D body surface? To answer that, multiple simulations were performed on revolutions bodies generated with different exponentials values to study the behavior of the pressure distribution and find the most appropriate exponent to use for the transformation of airfoils into bodies of revolution.

$$100 \cdot \frac{r}{l} = \left(100 \cdot \frac{y}{c}\right)^{1.17} \tag{3.2}$$

To have a better perception of the influence of the exponent value, the simulations were run without the ground wall condition to be more similar to the airfoil flow condition. However these simulations were performed after the construction of the vehicle due to the tight deadline for the competition. That means the vehicle was designed with the equation (3.1), and all the conclusions of the exponential value influence analysis will be available for implementation in future works on the vehicle body development.

3.1.2 Concept Implementation

In a first stage it was necessary to define the pilot position based on a good ergonomic position and also on the SEM 2014 rules [31], such as the visibility requirements. For that, the driver position was studied and implemented (see Figure 3.3).

Note that, at that time, the team pilot was quite a big person for the job, 1.69m tall, compared with the typical top team pilot. This fact contradicted a fundamental design concept that it is usually present in any good aeronautical engineering design: the best streamlined shape body can be even better if made smaller, it will have even smaller drag.

Figure 3.3 – 3 Views of pilot position a) Front view b) Side View c) Top View

With the pilot position defined in 3 views it was possible to export the driver position to CATIAV5R20 and start the first vehicle design stage. This first design was created to evaluate the space needed and study the placement of the various internal components, *e.g.* the wheels, which in this case were two front steering wheels and one propulsive rear wheel. It were also followed the SEM 2014 rules, where on Chapter 1 article 39 they dictate the limits of dimensions for the vehicle body [31]. This tadpole vehicle configuration was later changed to tricycle for implementation of an innovative vehicle tilting steering system to eliminate tire cornering drag. This limitations can be consulted on Appendix A - Table A.1. Like shown in Figure 3.4 and Figure 3.5, the initial vehicle design shows the effort of reducing the size while respecting the basic principles of streamlined vehicle aerodynamics in preventing any boundary layer separation, above all, eliminate bluntness in the after body shape.

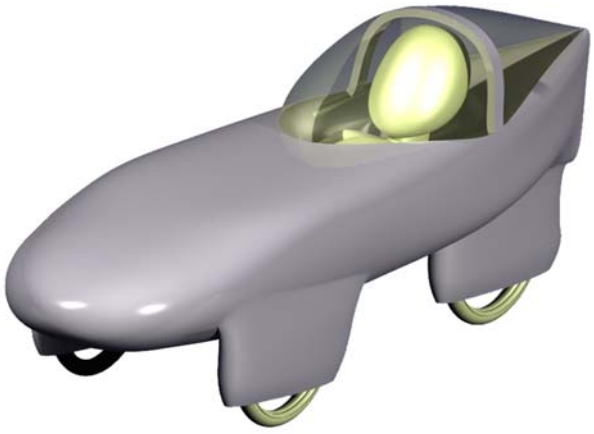

Figure 3.4 - 3D view of first design of the vehicle configuration concept

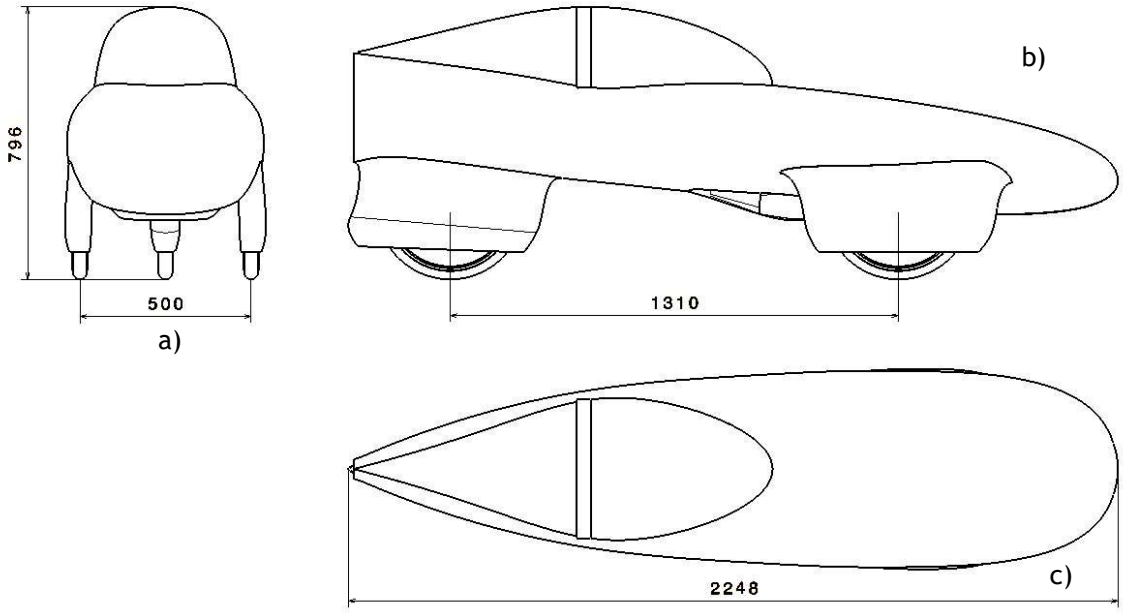

Figure 3.5 - 3 Views of first design of the vehicle configuration concept. Dimensions in [mm] a) Front View b) Side View c) Top View

The next step was to evaluate the cross section area distribution along the longitudinal axis of this initial body design. For that, a series of transversal planes separated of 10mm along the longitudinal axis. As each plane was created, the vehicle was cut by it to create transversal cross sections (see Figure 3.6).

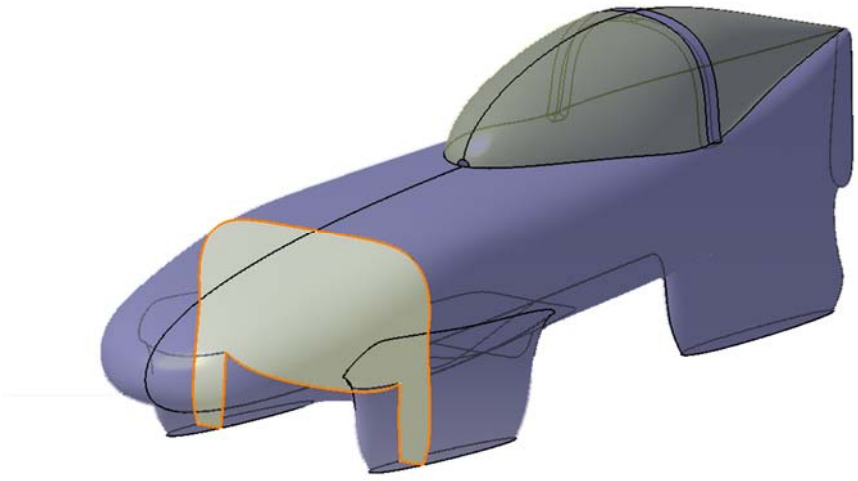

Figure 3.6 - Example of transversal section

Each cross section has an associated area calculated with the CATIA V5 *Measure Item* tool. In order to compare the vehicle cross section area distribution to that of an airfoil, it was defined the equivalent body of revolution of the initial body by using equation (3.3) to calculate each cross section radius.

$$r_{car}(x) = \sqrt{\frac{A_{section}(x)}{\pi}} \tag{3.3}$$

where,

$r_{car}(x)$ – Section radius $[m]$
$A_{section}(x)$ – Transversal area of the section obtained with CATIAV5 $[m^2]$

With this data the graphic on Figure 3.7 was constructed, which represent the equivalent body of revolution corresponding to the initial body design. Note that the effort to produce an initial streamlined design is not so clear in the body of revolution as it was (compare with Figure 3.5). With the required equivalent body of revolution to satisfy the internet volume needs it was possible to search for the suitable airfoil to match the overall required radius distribution of the vehicle.

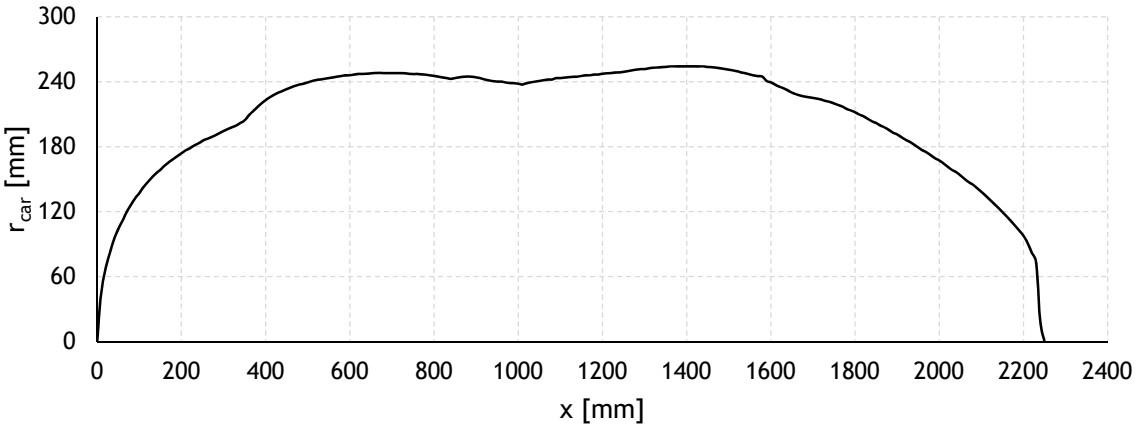

Figure 3.7 – Equivalent body of revolution of the initial design

3.1.2.1 Airfoil Selection

The airfoil selection was constrained by the following criteria:

- Symmetric Airfoil;
- Low drag value;
- Low friction value;
- Good pressure distribution with late transition.

If Galvão's theory is right [1], it will be possible to maintain the airfoil properties for the new design 3D body of revolution. To begin the airfoil selection, it is necessary to calculate the Reynolds number where the vehicle will operate, equation (3.4), in order to have a design point.

$$Re = \frac{\rho \cdot U_{car} \cdot L}{\mu} \tag{3.4}$$

Where:

Re – Reynolds number

L – Vehicle length $[m]$

U_{car} - Vehicle velocity $[m/s]$

μ – Dynamic viscosity $[N \cdot s/m^2]$

To define U_{car} it is necessary to follow SEM rules. On chapter 2 of official SEM rules under article 123 [32] it is said: *"For their attempt to be validated, teams must complete ten laps in a maximum time of 39 minutes with an average speed of approximately 25 km/h."* [32].It is also important to define the allowed length interval for the vehicle's body. For that, it was defined 2200mm as the minimum length, which is an approximated length of the initial design and 3500mm for the maximum length, which is the maximum length permitted by the rules. In Table 3.1 the data used to calculate the Reynolds range for the vehicle is shown.

Table 3.1 - Data for the calculation of the vehicles body Reynolds number

U_{car}	$25\ km/h \cong 7\ m/s$
L_{min}	$2200mm = 2.2m$
L_{max}	$3500mm = 3.5m$
ρ	$1.225\ kg/m^3$
μ	$1.827 \times 10^{-5}\ N \cdot s/m^2$

With this data the new body Reynolds number range is:

$$Re = [1024372; 1629682]$$

After defining the Reynolds range it is possible to start the study of multiple symmetric airfoils. For that, an analysis tool was used that can analyze airfoils that operate at low Reynolds numbers. The tool was XFOIL [33] through XFLR5 [34] interface. XFOIL is a proven airfoil design and analysis tool [35].

To start an analysis it is necessary to input the airfoil coordinates on the software via DAT files. Those airfoil files can be consulted and downloaded at the UIUC Airfoil Data Site [36]. The first selected airfoils were some well-known airfoils to see how they behave for our range of Reynolds and to check the coordinate distribution of those transformed airfoil with the radius distribution of the initial body vehicle design. However, since the vehicle configuration changed for one propulsive front caster wheel and two tilting rear wheels, it was decided to try the design of a new airfoil in order to get a lower drag coefficient, with an extensive laminar region and an appropriate transformed airfoil radius distribution. The cr001 airfoil was a start point to create a suitable airfoil, where the upper surface of airfoil was used to create the symmetric version of the airfoil. After loading the DAT file of the symmetric upper surface of cr001 on

XFLR5, the airfoil modification proceeded using the direct inverse design to change the pressure coefficient profile resulting in a changed thickness distribution, camber line and trailing edge thickness (see Figure 3.8).

After each modification of the airfoil a direct analysis was performed to compare the generated airfoil with the existing airfoils, to perform this analysis some parameters were defined to simulate the vehicle conditions. One of these parameters is the Reynolds number range who was already calculated, and the other is the turbulence level, NCrit [37]. It translate the freestream turbulence level effect on the boundary layer transition model, the lower is this number the higher is the effect of turbulence. The standard and commonly used value for this parameter is NCrit=9 (see Table 3.2), but for the present study case NCrit=2 was chosen to simulate the turbulence caused by the body surface imperfection and road induced vibration of the vehicle body. The analysis were ran with fixed airspeed and within a small angle of attack range. The process of modifying the airfoil and checking the respective transformation into a revolution body against the required internal volume of the initial design continued iteratively until a satisfactory solution was found.

Table 3.2 - Typical values of NCrit for various situations [37]

Situation	NCrit
Sailplane	12-14
Motor glider	11-13
Clean wind tunnel	10-12
Average wind tunnel	9
Dirty wind tunnel	4-8

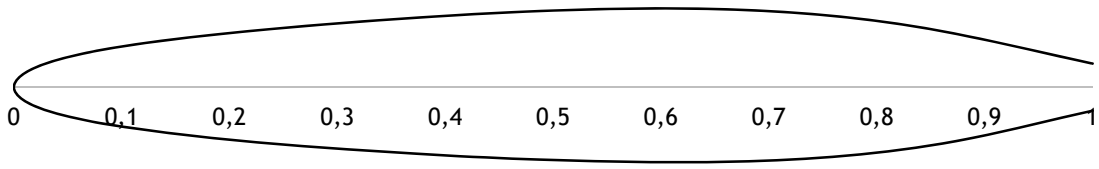

Figure 3.8 – Airfoil created on XFLR5 for the vehicle design

To validate the airfoil other airfoil were also analyzed with thick trailing edge and thickness modifications. The thick trailing edge was found to be a compromise in terms of drag increment and suitability of the transformed airfoil to the required cross section area distribution of the initially designed body. In graphic of Figure 3.9, the drag coefficient is lower on final solution airfoil than the others, and also has a lower variation of the drag coefficient with the angle of attack, thereby achieving the goal of low drag. Figure 3.10 shows that AERO@UBI airfoil has a

larger laminar zone extension for higher angles of attack, despite the AH 79-100 A mod having a lower drag coefficient at 0° angle of attack. With the airfoil selected it is possible to apply the transformation to evaluate the cross section area distribution compatibility of the final revolution body versus the initial body design equivalent revolution body. In Figure 3.11 the transformed airfoil was translated to the left (moved forward of the initial design nose position) to have a better match in the cross section area distribution and it was also applied a thickness factor of 0.84 on vertical coordinate, modifying the thickness of the airfoil to better match the transformed airfoil cross section are distribution to that required by the initial body design. This transformations does not affect the properties of the airfoil, only the module of the pressure coefficient changes but not the drag characteristics. A flowchart of all the process of airfoil selection is shown on Appendix B - Figure B.1, giving a better understanding of the process.

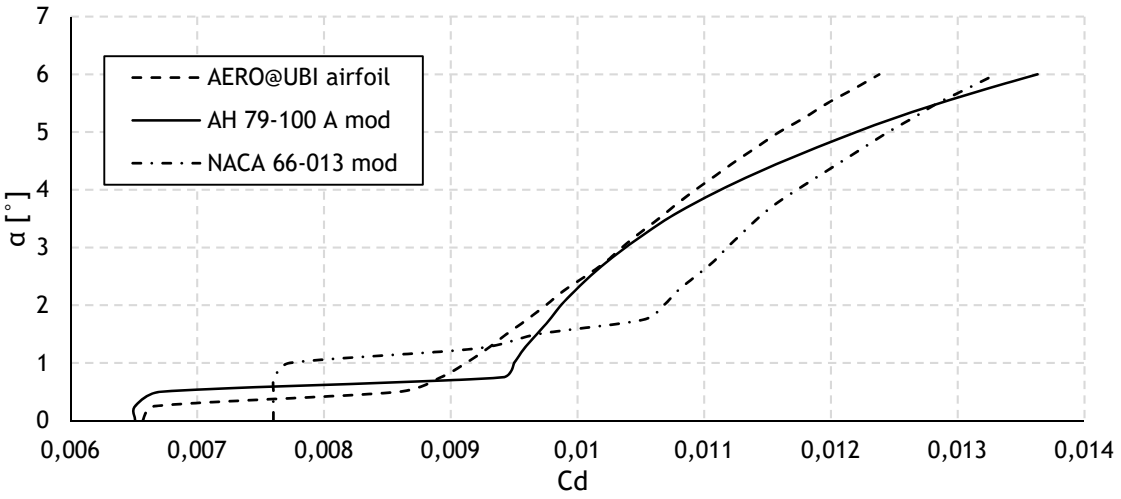

Figure 3.9 - Variation of Drag coefficient with angle of attack[3] Re=1500000

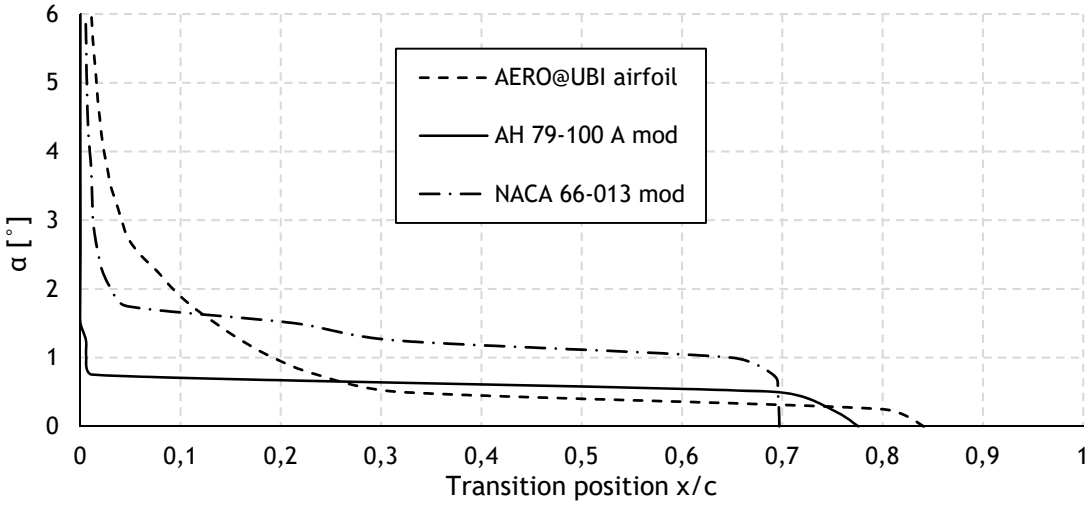

Figure 3.10 - Longitudinal position of the boundary layer transition[3] Re=1500000

[3] Data extracted from XFLR5

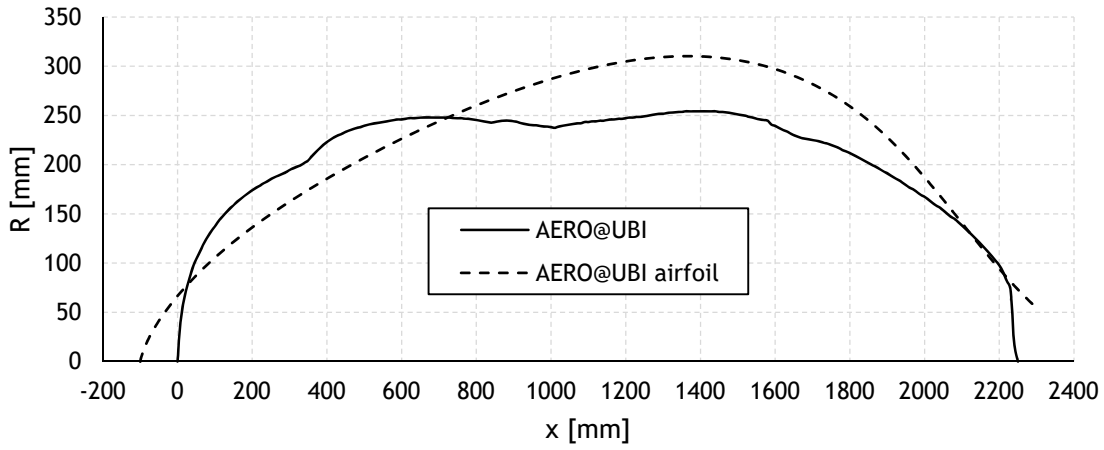

Figure 3.11 - Coordinate distribution

3.1.2.2 Vehicle Body Design

The objective of this method is to create a 3D body of revolution from the transformed selected airfoil and modify this body of revolution to a new 3D equivalent body adapted to the internal volume shape requirement by changing each cross section shape but maintaining the corresponding cross section area. To help the design of the vehicle body the first modification to the transformed airfoil 3D body of revolution was to camber the symmetry axis to better comply with the pilot position, while trying to end with a positive camber to prevent the generation of lift due to ground interference in the flow. By doing so, all cross sections continued to be circles. The created pseudo revolution body with a deformed axis is shown in Figure 3.12. This first shape helped to give a first idea of the final body shape and also served as a support to compare the cross section areas as each section was being changed to its convenient shape.

The final vehicle body shape was created with multiple cross sections spaced by $6cm$ (see Figure 3.13) along the longitudinal axis since the actual construction of the vehicle body was made from $6cm$ roofmate boards that were cut with a four axis CNC hot wire cutting machine and glued between them. The use of CATIAV5 *Multi-Sections Surface* tool gave a shape with some irregularities. This was mostly the result of iteratively changing each cross section shape while trying to respect the prescribed cross section area distribution. In the actual vehicle body, the final shape smoothing was performed with sand paper. To realize the CFD study, it was necessary to correct the shape. This was performed with another software: Blender. It is an open source 3D creation suite [38] commonly used by designers and movie industry but also used by engineers as a CAD tool to optimize the quality of surfaces. The shape was exported from CATIAV5R20 in STL format to Blender, and modifications were made to smooth the final body surface to get as close as possible to the actual prototype (see Figure 3.14).

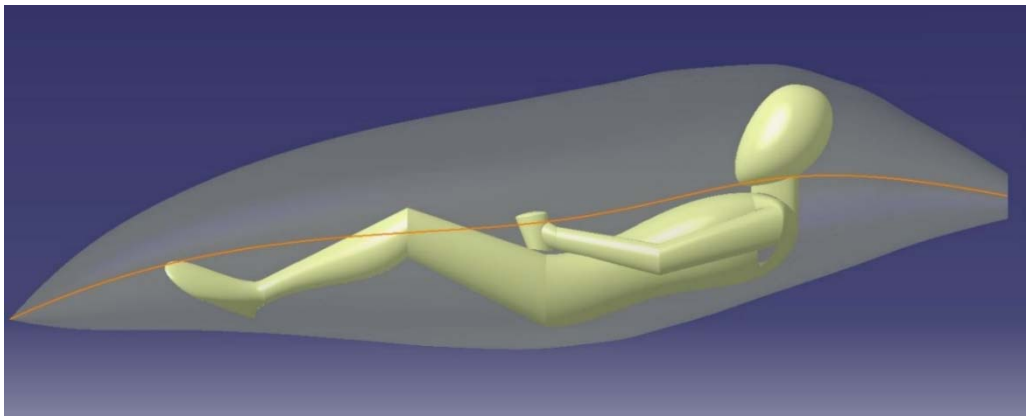

Figure 3.12 - Lateral view of asymmetric body created for support design

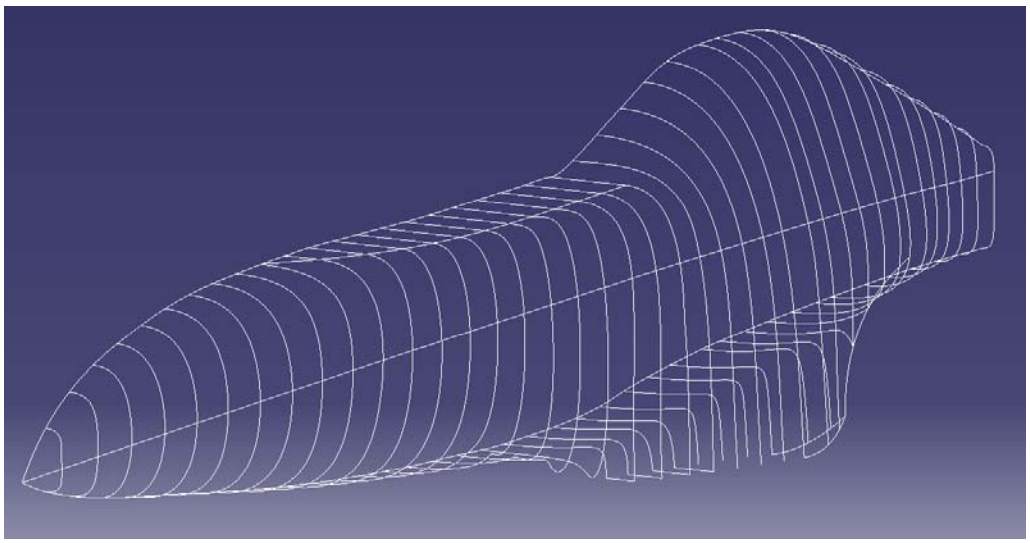

Figure 3.13 - Multiple section sketch of AERO@UBI

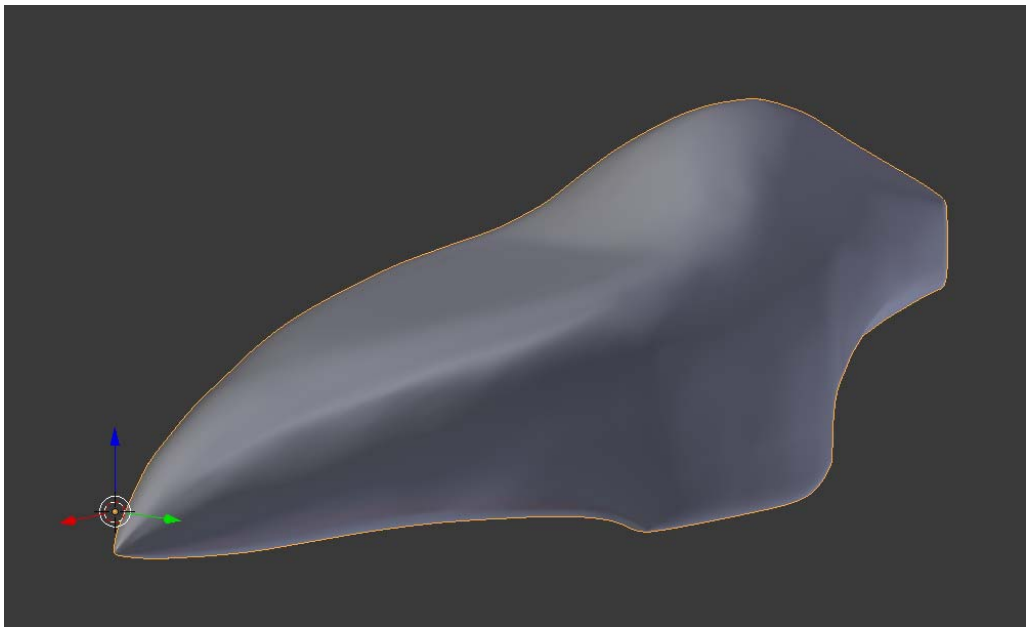

Figure 3.14 - Vehicle shape after some sculpt modifications on Blender

For this project it was necessary to exclude the wheels and their cavities due to the high mesh complexity that would result and the available computational resources. With that, some modifications on vehicle shape to be possible to make a CFD simulation, these modifications consisted mainly on closing the wheels cavities (see Figure 3.15). On future works it advised to simulate a single wheel with a cavity, or even the whole assembly, to evaluate the impact on vehicle aerodynamics performance.

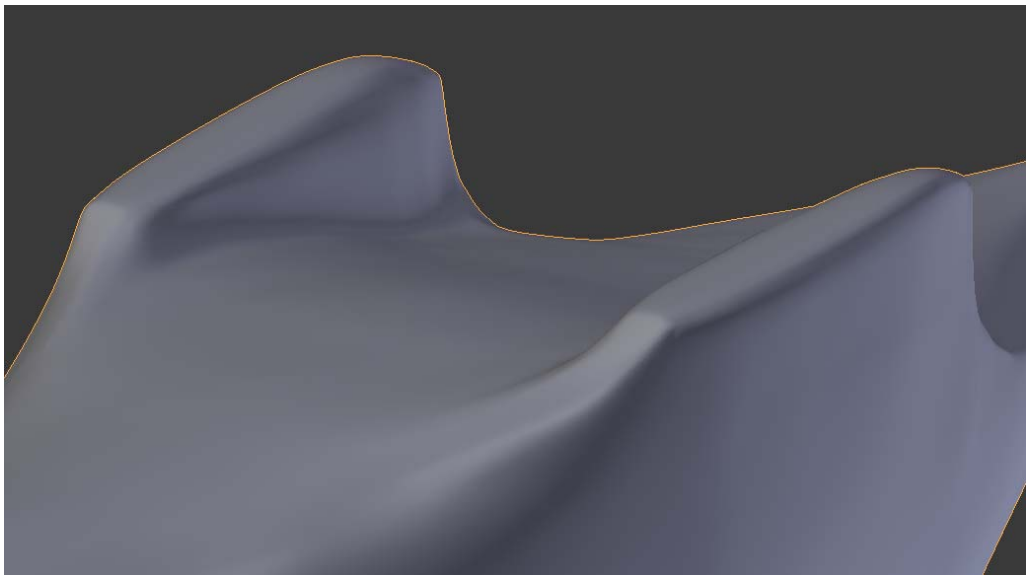

Figure 3.15 - Closed cavities for CFD simulation

With the final body design it was evaluate once again the coordinate distribution. As it is possible to see in Figure 3.16 the distribution of the present body vehicle is almost equal to the transformed airfoil. The comparison with the actual prototype was not performed

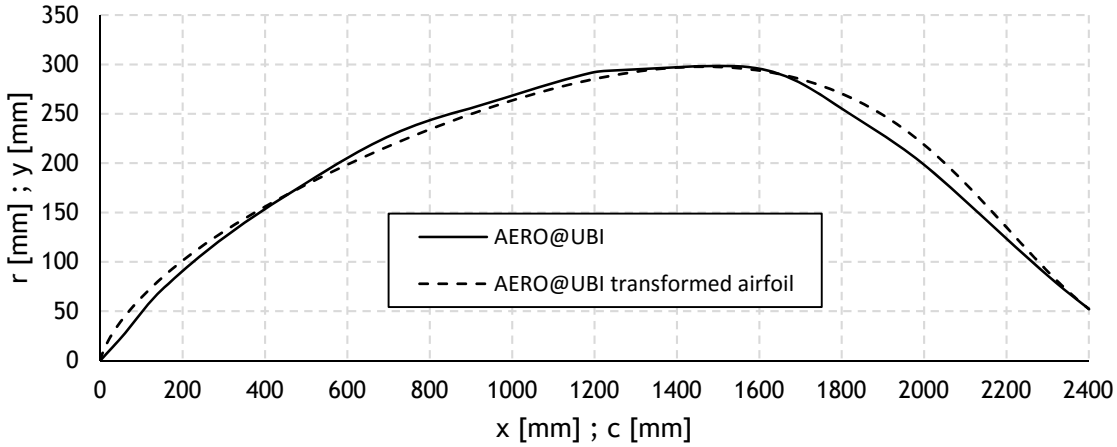

Figure 3.16 - Final coordinate distribution of the vehicle

3.2 Grid Generation

For this simulation the mesh was created with the HELYX-OS software. This software is an open source Graphical User Interface (GUI) with the OpenFOAM developed by Engys [39]. Using HELYX-OS a basic mesh is created and the software controls snappyHexMesh, an advanced meshing tool of OpenFOAM which is able to mesh the geometry from STL files [40]. Andrew Jackson on 7th OpenFOAM workshop 2012 gave a good explanation about the parameters available on snappyHexMesh [41]. It would be possible to perform all the simulation using HELYX-OS and the OpenFOAM suit but it was opted to use ANSYS Fluent, as solver for the created mesh.

3.2.2 Grid Generation Process

The use of a suitable mesh for the CFD simulation is important in order to have a valid result. For that, the choice between a structured mesh and an unstructured mesh needs to be made. For a complex geometry an unstructured mesh is faster to create than a structured mesh. However the structured mesh results in a better algorithm to store data, adding/subtracting 1 from cell indices (see Figure 3.17), it have less computational memory storage demand and therefore lower convergence time [42]. Also, with a structured mesh it is possible to have the cell aligned with the flow, helping further on the convergence time.

$i-1$	$j+1$	$i+1, j+1$	$i+1 j+1$
$i-1 j$	ij	$i+1 j$	
$i-1 j-1$	$ij-1$	$i+ij-1$	

Figure 3.17 - Structured mesh representation - $U(i,j)$ ⇐ data stored on a 2D array

One of the advantages of HELYX-OS is the simplicity of creating a structured mesh, where it is possible to add layers around the body to have a better mesh resolution within the boundary layer and also the possibility to refine the mesh on a desired region where intense gradients are expected.

Like explained in Section 2.2.4, in order to have a valid result, the blockage ratio should to be lower than 7.5%. For that it is necessary to give suitable dimensions to the control volume. In Figure 3.18 it is shown how the control volume has been defined to minimize the blockage effect, where L is the vehicle's length.

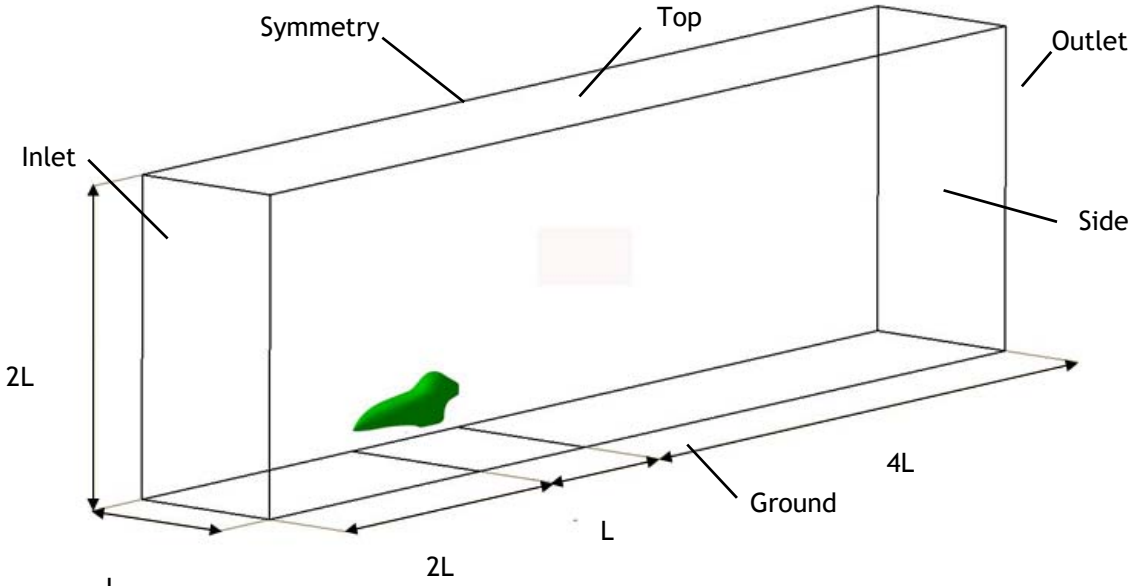

Figure 3.18 - Dimensions for control volume (half body) and boundary mesh labels

With the control volume defined the next step is the creation of the mesh in HELYX-OS. The first step in HELYX-OS is the creation of the control volume bounding box. In Figure 3.19 it is shown how this box is defined in the software, where all the values have as origin the origin of the CATIAV5 design.

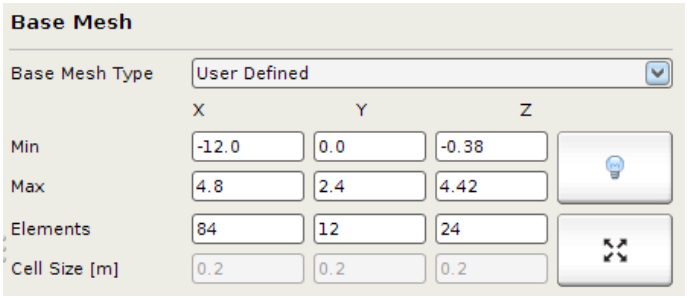

Figure 3.19 - Bounding box definition

To have a better mesh it is recommended to create a mesh where cells are perfect cubes, equation (3.5) demonstrate how the number of elements was calculated to have the same cell size in each axis. This is criteria used to create the basic mesh.

$$\frac{|maxX - minX|}{n_x} = \frac{|maxY - minY|}{n_y} = \frac{|maxZ - minZ|}{n_z} \quad (3.5)$$

where,

$maxX$,$maxY$ and $maxZ$ - maximum distance from the references plans for each axis

$minX$,$minY$ and $minZ$ - minimum distance from the references plans for each axis

n_x, n_y and n_z - number of elements for each axis

The values for Z axis were defined according to the car height from the road, since the wheels are not present for the simulation. The value of cell size was decided to be 0.2m, since the flow away from the vehicle doesn't need a high resolution, which means a reduction on cell number. After that the next step is to import the STL file of the body vehicle to HELYX-OS (Figure 3.20) and label the mesh boundaries (see Figure 3.18) for later use to define the boundary conditions.

As mentioned, HELYX-OS mesh creation is based on snappyHexMesh. To refine the mesh around the surface of the body, the cells are split by levels, that is, HELYX-OS will divide the cells in half based on equation (3.6) thus giving the surface cell size.

$$SCS = \frac{BBCS}{2^{RL}} \tag{3.6}$$

where,

SCS - Surface Cell Size $[m]$ RL - Refinement Level

$BBCS$ - Bounding Box Cell Size $[m]$

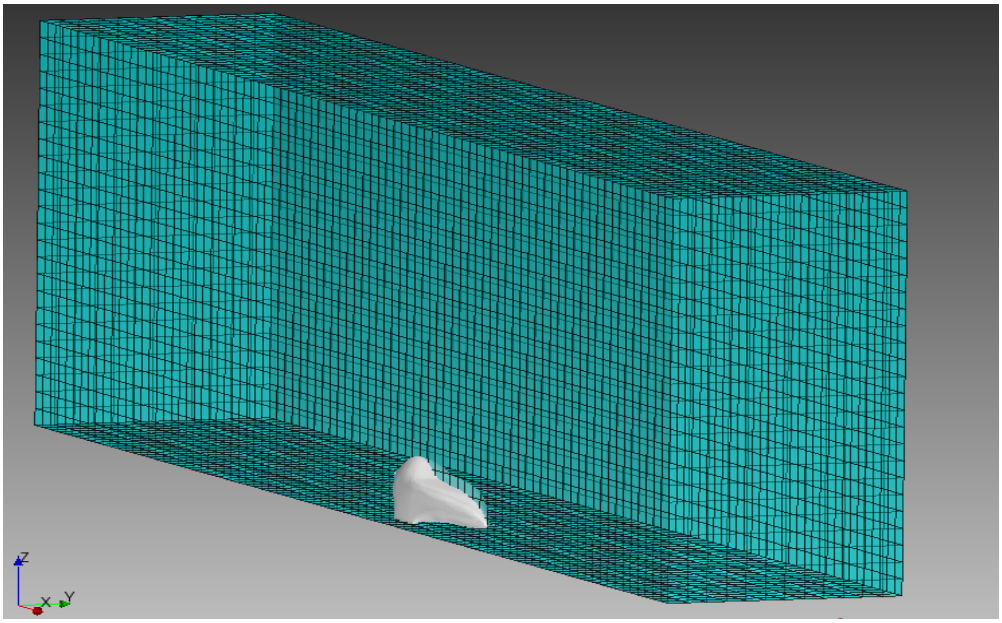

Figure 3.20 - Position of the vehicle body on the control volume bounding box

The desired refinement levels for the body are defined like shown in Figure 3.21. The first level (on the left box) is designed as the minimum level which corresponds to the level applied for the cell that will cross the surface. The second level (on the right box) is called maximum level. This is applied on cells that can see intersections that form an angle in excess of that specified by the software (by default 30°). Figure 3.22 shows the influence that the refinement levels has in the mesh.

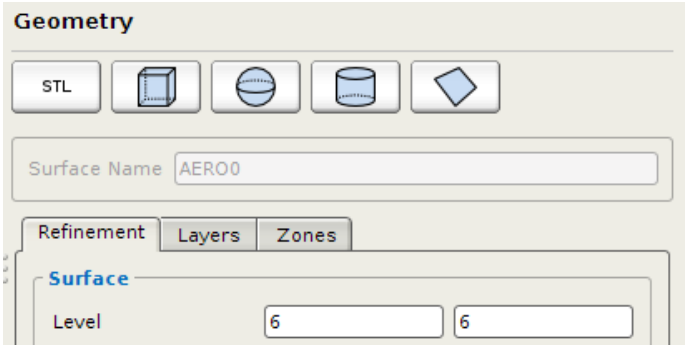

Figure 3.21 - Surface refinement level definition for the body

The most critical aspect of a mesh is the creation of layers to reach the desired value y^+ of the first cell nest to the vehicle body. Before creating the layers on HELYX-OS, it was necessary to calculate a first value of the first cell height for a corresponding $y^+ = 1$. For that, the Pointwise online calculator was used (see Figure 3.23) [43]. According to the calculator in order to achieve a value of $y^+ = 1$, the first cell height must be approximately $50\mu m$. Figure 3.24 shows the layer setup on HELYX-OS, where the final layer thickness parameter is the ratio between the last layer thickness (the layer in contact with the body surface) and the SCS of the body surface. To help to define the correct determination of the final layer thickness parameter value, the equation (3.7) was deduced. The layer minimum thickness parameter is the ratio between minimum layer thickness desired for the body surface and the SCS, however it was left in blank to have a constant layer growth and to avoid a conflict on parameters and so avoid errors on the mesh. Layer stretching is the expansion rate of the layers starting from the surface. Due to the complexity of the body and computational limitation only 84,6% of the total layered surface was created (see Figure 3.25), which means that some parts of the body do not have layers or do not have the totality of the prescribed layers (see Figure 3.26).

$$RFLT = \frac{\Delta E^{(n_{layer}-1)} \cdot \Delta s^*}{SCS} \tag{3.7}$$

where,

$RFLT$ – Relative Final Layer Thickness

ΔE – Expansion Rate

n_{layer} – Number of Layers

Δs^* - First cell height

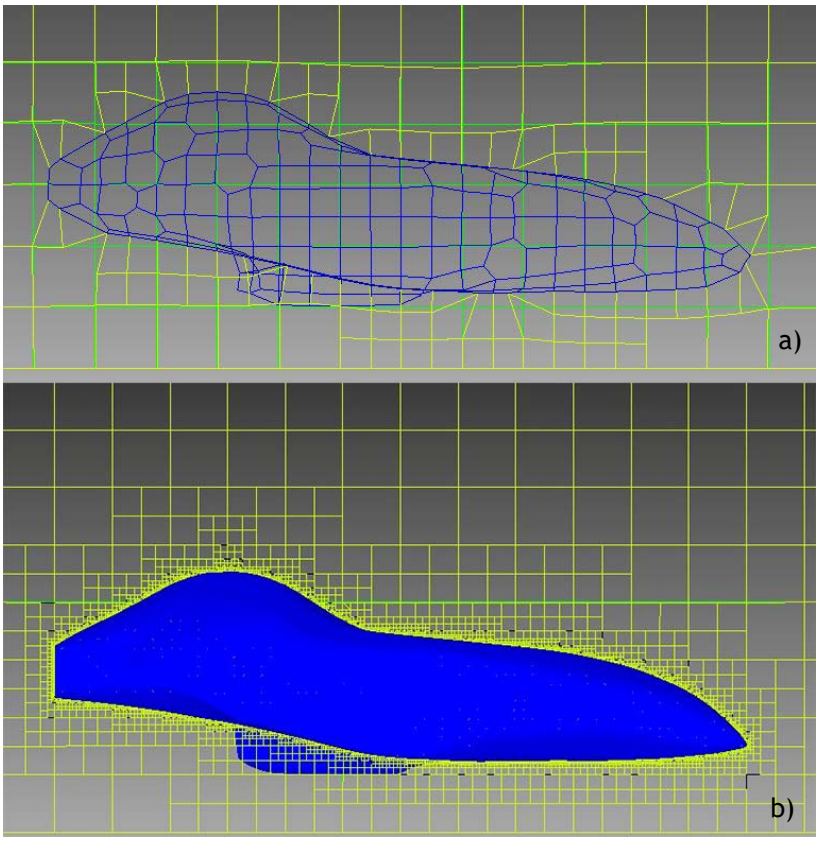

Figure 3.22 - a) Level 1 of surface refinement b) Level 2 of surface refinement

Input

Reset to Sea Level Conditions

U_∞:	7	freestream velocity (m/s)
ρ:	1.225	freestream density (kg/m3)
μ:	0.000018375	dynamic viscosity (kg/m s)
L:	2.4	reference length (m)
y^+:	1.0	desired y^+

Output

Compute Wall Spacing

Δs:	0.000050828646422924	wall spacing (m)
Re_x:	1120000.0000000002	Reynolds number

Note: -1 indicates an input error

Figure 3.23 - Pointwise online Y+ calculator

Refinement | Layers | Zones

Number of Layers	10
Final Layer Thickness	0.08
Layer Min Thickness	
Layer Stretching	1.2

Figure 3.24 - Layer definition

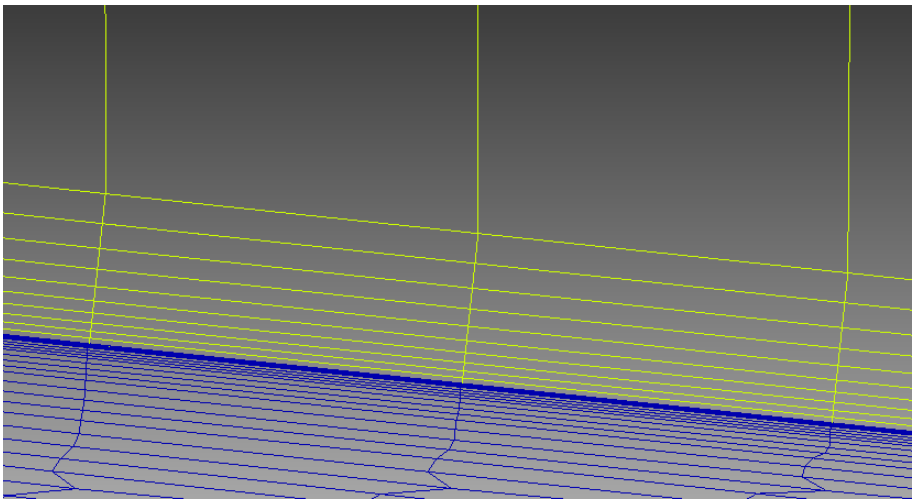

Figure 3.25 - Detailed view of created layers on the body surface

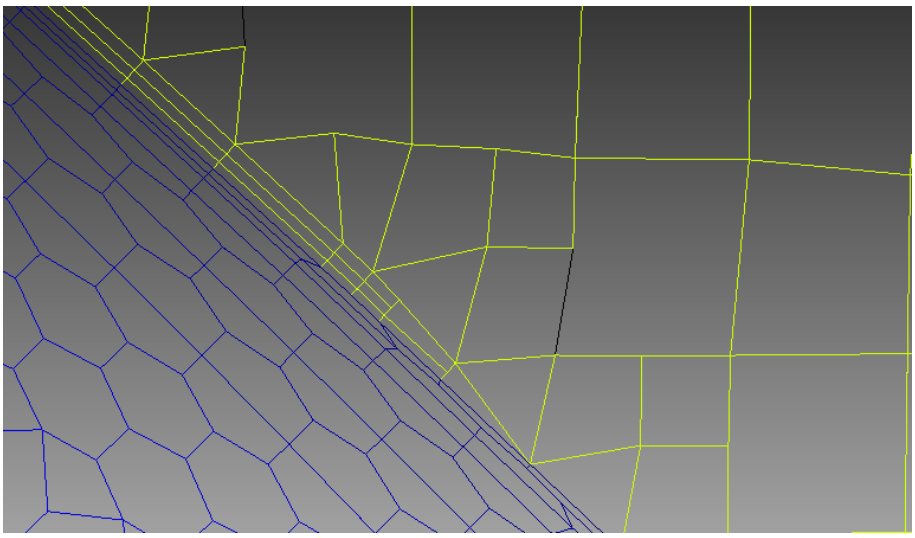

Figure 3.26 - Detailed view of missing and deformed layer zones

The next step was the refinement of the mesh in some important regions of the flow where high gradients values could be expected in the flow, such as: around the body surface; the wake of the vehicle; the nose and the ground. To refine the mesh around the body surface it was defined a refinement level from a certain distance from the body (see Figure 3.27). To realize the rest of refinements some geometric volumes, with refinement levels prescribed inside, were created (see Figure 3.28). For the wake, a cylinder was added at the rear of the body till the end of the control volume with a level 2 of refinement. At the nose, a sphere was also added with level 2 of refinement. Finally, for the ground, it was added a parallelepiped under the car in contact with the ground boundary with a level 2 of refinement. The final result for the mesh is shown in Figure 3.29. To be able to use this mesh on ANSYS Fluent, it is necessary to convert it. Through the command line *foamMeshToFluent* it writes out the created OpenFOAM mesh in ANSYS Fluent mesh format.

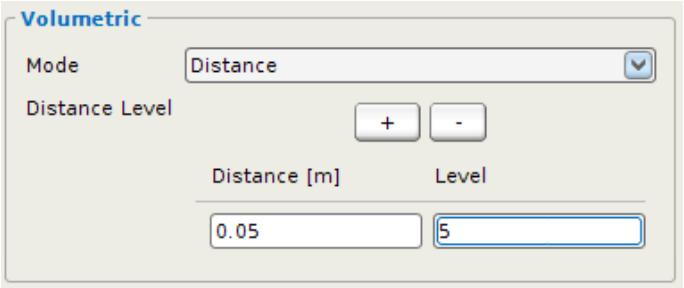

Figure 3.27 - Definition of cell refinement from a given distance

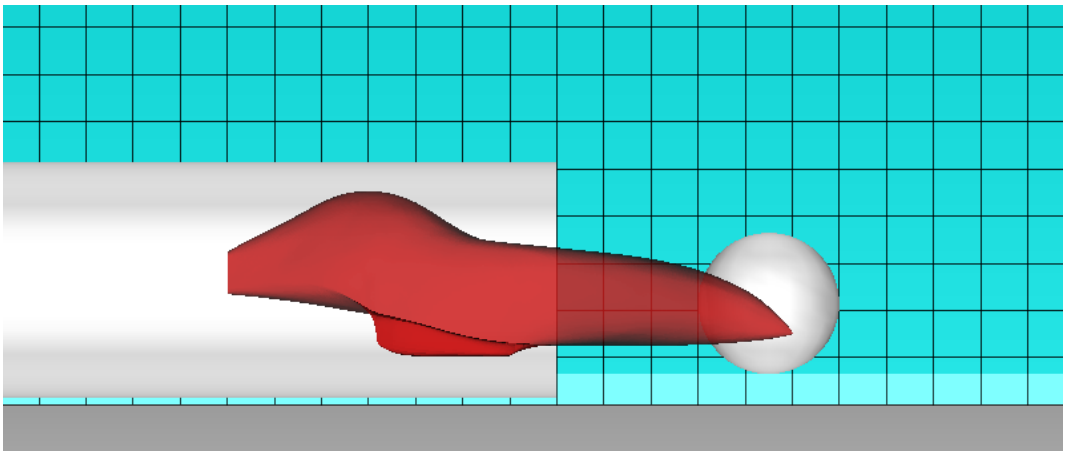

Figure 3.28 - Geometrics figures for zone refinement

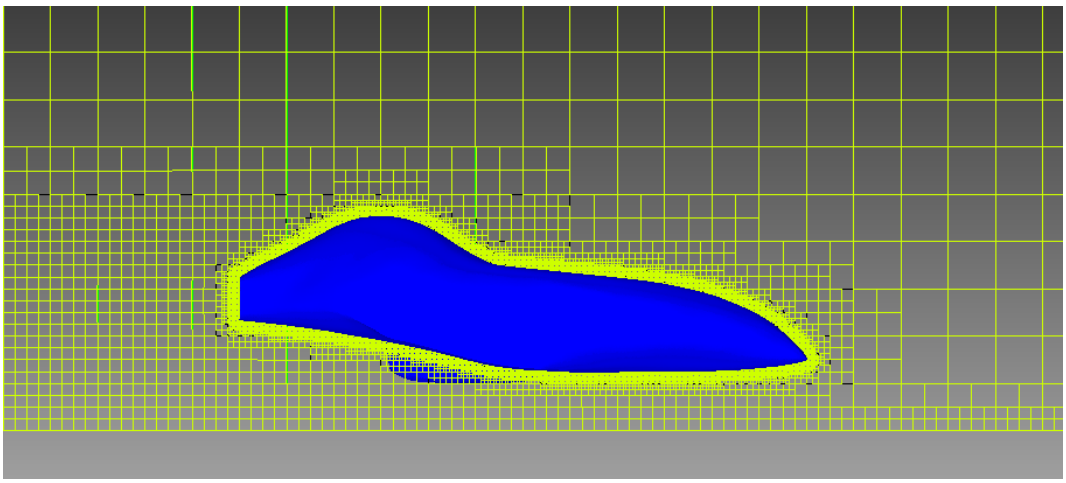

Figure 3.29 –Detailed view of mesh result from HELYX-OS

3.2.3 Mesh Analysis

The mesh generated by HELYX-OS was analyzed to control its quality. HELYX-OS has defined parameters of quality such as skewness angle and the cell volume, the mesh is generated when all these parameters are met. These parameters can be modified by the user, but in this case they were left with the default setting to give a robust mesh. Also an important parameters to

control is the body surface cells y+ values. As shown in Figure 3.30 the mesh was generated fulfilling all the quality parameters.

```
patch   faces    layers   overall thickness
                           [m]       [%]
-----    -----    ------   ---       ---
AERO@UBI 169980   6.42     0.00106   84.6

Layer mesh : cells:1930032  faces:6130191  points:2292759
Cells per refinement level:
    0   22363
    1   6156
    2   64321
    3   6568
    4   23999
    5   371413
    6   1435212
Checking final mesh ...
Checking faces in error :
    non-orthogonality > 65  degrees                          : 0
    faces with face pyramid volume < 1e-13                   : 0
    faces with face-decomposition tet quality < 1e-15        : 0
    faces with concavity > 80  degrees                       : 0
    faces with skewness > 4   (internal) or 20  (boundary)   : 0
    faces with interpolation weights (0..1)  < 0.05          : 0
    faces with volume ratio of neighbour cells < 0.01        : 0
    faces with face twist < 0.02                             : 0
    faces on cells with determinant < 0.001                  : 0
Finished meshing without any errors
```

Figure 3.30 - Log file from HELYX-OS

To check the y+ value, the flow simulation has to be completed first since it depends on wall shear stress. After the simulation it is possible to evaluate the y+ values on the vehicle surface. As shown in Figure 3.31, some parts of the car (especially the nose) have a y+ value higher than 1, reaching not more than 20% of the surface of the body. It is seen that the highest value of y+ is 60.5 which is acceptable to run the flow simulation to a valid solution.

All the previous analysis were performed on all the simulations, validating them and modifying different parameters like the level of refinement or the RFLT in case of the y+ value were too high to achieve the solution validity.

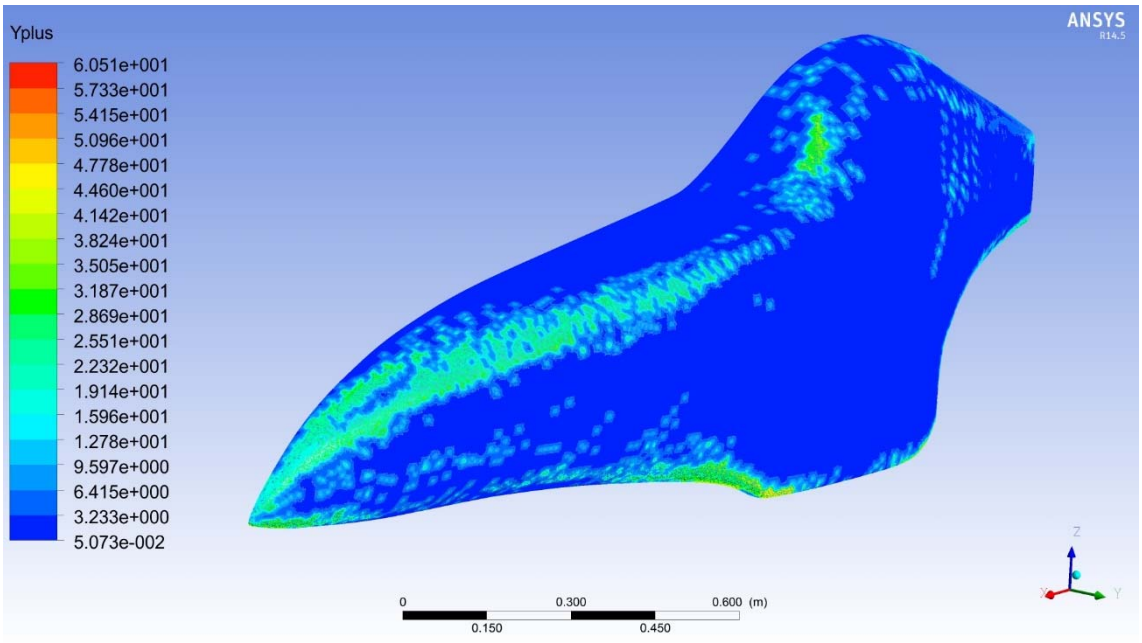

Figure 3.31 - Wall y+ distribution in the half vehicle surface

3.3 CFD Simulation Setup

The CFD simulation was performed with ANSYS Fluent 14.5. In Section 2.2.6 it was explained the importance of the verification and validation of CFD simulation, and the use of benchmarks cases suited for the flow case of study. Through the benchmark Ahmed body simulation it was possible to define the correct parameters to our simulation of AERO@UBI vehicle.

3.3.1 Solution Setup

The first step was importing the mesh previously converted from OpenFOAM mesh to Fluent mesh. For this simulation K-ω SST turbulence model was used. The Shear-Stress Transport (SST) K-ω model was developed by Menter [44] to combine the robust and accurate formulation of the K-ω model in the near-wall region and the K-ε model behavior in the rest of the flow field. The superior performance of this model has been demonstrated in a large number of validation studies [45] [46]. The crucial part of the CFD simulation setup is defining correctly the boundary conditions. On Table 3.3 are shown the boundary conditions implemented for the present study case.

Table 3.3 - Boundary Conditions

Vehicle Body	Wall – No Slip
Ground	Wall – No Slip
Side, Symmetry and Top	Symmetry
Inlet	Velocity Inlet
Outlet	Pressure Outlet

The inlet boundary was defined with an airspeed vector normal to it with a value of $7m/s$ corresponding to the vehicle cruise speed. The turbulence specification was defined by the intensity and length scale, where the intensity has the value of 1% and the length scale of $0.08m$. The definition of the turbulence specification parameters was based on reference [15]. However the definition for external flows are not quite specific, so the values were defined by trial and error and comparison with the benchmark simulation. In order to maintain the atmospheric pressure in the outlet boundary the gauge pressure was defined to zero. The turbulence specification are the same as the inlet.

After defining the boundary conditions it was necessary to define the reference values for the correct calculations of the body forces coefficients. Since only half the body is simulated, the reference area was defined with half the frontal body area, the length correspond to the length of the vehicle (see Table 3.4).

Table 3.4 - Reference Values

Area	$0.17375\ m^2$
Density	$1.225\ kg/m^3$
Enthalpy	$0\ j/kg$
Length	$2.4\ m$
Pressure	$0\ Pa$
Temperature	$288.16\ K$
Velocity	$7\ m/s$
Viscosity	$1.7894 \times 10^{-05}\ kg/m \cdot s$
Ratio of Specific Heats	1.4

3.3.2 Solution Methods

The simulation is set to pressure-based solver. The pressure-based solver solve a pressure equation in order to satisfy the mass conservation of the velocity field (continuity). The pressure equation is derived from the continuity and the momentum equations. The scheme used to solve the pressure equation was the Coupled Algorithm. The coupled scheme obtains a robust and efficient single phase implementation for steady-state flows, with superior performance compared to the segregated solution schemes. In Figure 3.32 it is possible to see that the only difference between the two algorithms is that the RANS momentum equations and continuity equation are solved in the same step, which means that the coupled algorithm has a better solution convergence compared to the segregated algorithm. However, the memory usage increase since the discrete system of momentum and continuity equations needs to be stored to solve the velocity and pressure fields. In [10] it can be found more information about these algorithms.

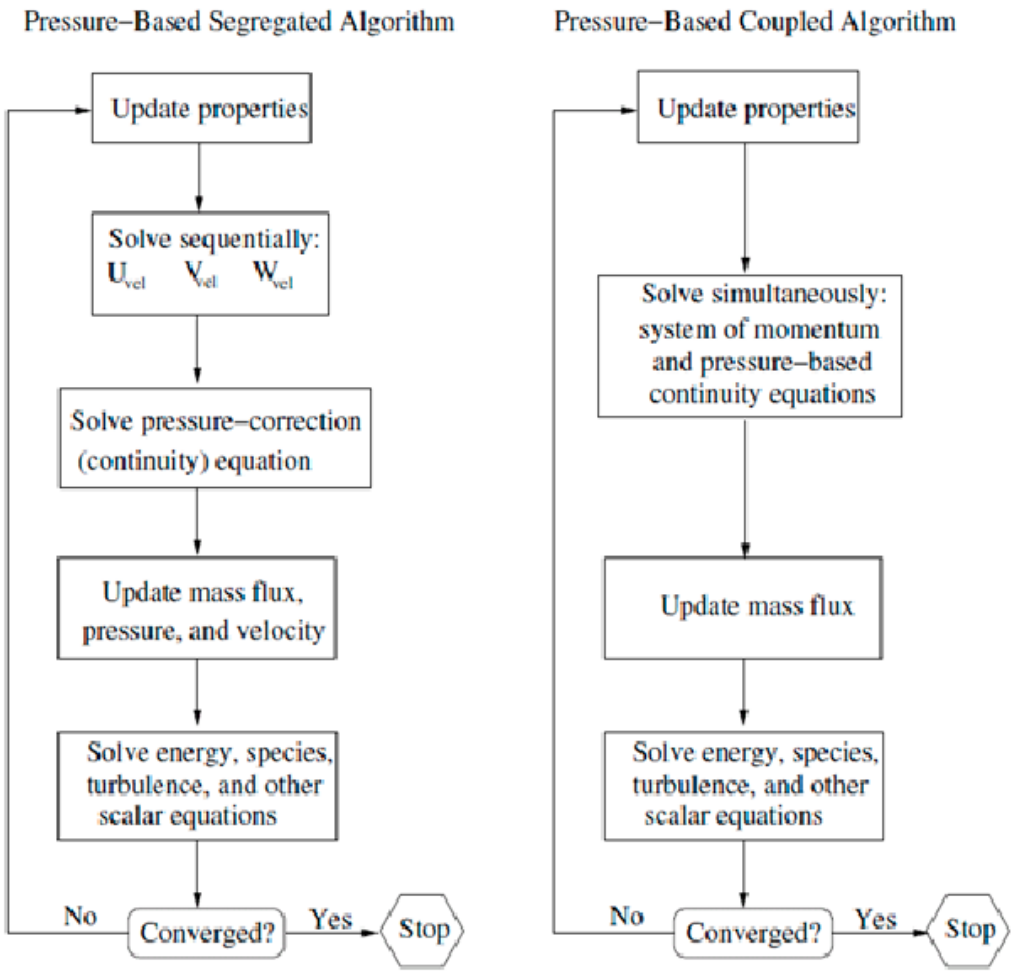

Figure 3.32 - Comparison of Pressure-Based Segregated Algorithm and Pressure-Based Coupled Algorithm [10]

To obtain a fastest and more robust solution the pseudo-transient solution method was selected, which is a form of implicit under-relaxation for steady-state case [47]. Under-relaxation factors are used to suppress oscillations in the flow solution that result from numerical errors, they decrease the speed of convergence but increase the stability of the calculation [48]. The values of pseudo-transient relaxation factors, used for the present case, are described on Table 3.5.

Table 3.5 - Pseudo Transient Explicit Relaxation Factors

Pressure	0.4
Momentum	0.5
Density	1
Body Forces	1
Turbulent Kinetic Energy	0.75
Specific Dissipation Rate	0.75
Turbulent Viscosity	0.95

To help the solution convergence the first 25 iterations were calculated with the first order of spatial discretization. However, from then on, to improve the accuracy of final solution the second order discretization was used.

To check if the solution converged it is necessary to control the solution parameters, these were the residuals, the mass flow rate and the drag and lift coefficients. The residuals are the difference between the previous iteration result and the current one of RANS momentum equations and continuity equation. All the values of residuals must be under 1×10^{-4} to have a good accuracy of solution and also need to show a stabilized value. The mass flow rate is calculated between the inlet and outlet boundaries, the difference between them must be inferior of 1% of the inlet mass flow. The value of drag and lift coefficients must converge to a single value to achieve the accurate result.

3.3.3 CFD Procedure Validation with the Ahmed Body

In this section the result of the validation simulation with the Ahmed body is shown. This case serves to validate the setup used for the present simulation.

Ahmed on 1984 realized an experimental work of a simple body where he studied the flow structure, and aerodynamic characteristics varying the rear slant angle - φ [18] (see Figure 2.12). To be possible the validation of this setup there exist two test case performed by Becker, Lienhart and Stoots [49] with a slant angle of 25° and 35°. The measurements where performed in the LSTM low-speed wind-tunnel with a bulk velocity of 40 m/s.

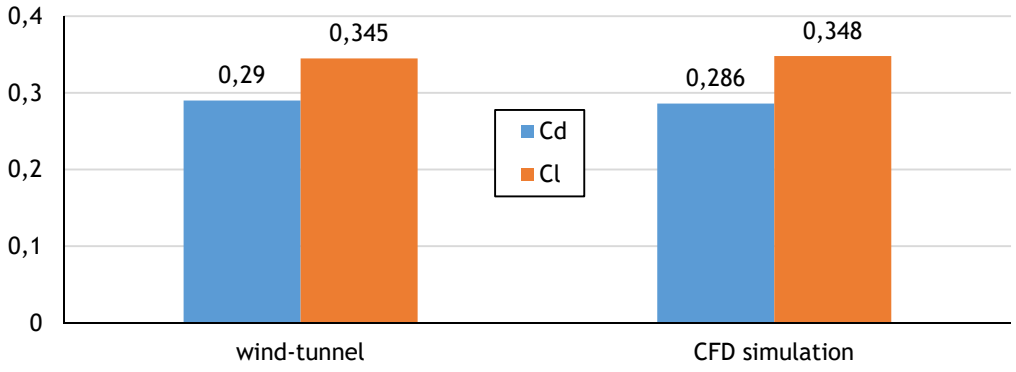

Figure 3.33 - Result comparison for Ahmed Body

To be able to compare the values, the present simulation of the Ahmed body was performed with a slant angle of 25° and a velocity of 40m/s. Figure 3.33 shows the results of the simulation. The results have an error smaller than 1% compared with the experimental data, which means that the CFD setup is valid to the present vehicle body simulation.

Chapter 4

4. Results and Discussion

In this chapter all the results from the CFD simulations undertaken with ANSYS Fluent on the created vehicle body design are presented. The results are in form of tables, plots and contour scenes, with their respective explanations. The post-processing was made on ANSYS Results.

4.1 Vehicle Analysis

To analyze the flow around the vehicle and test the airfoil transformation design concept it was needed to simulate the transformed airfoil body of revolution (see Figure 4.1). Different parameters are compared between the transformed airfoil body of revolution and the 2D airfoil to be able to verify the concept.

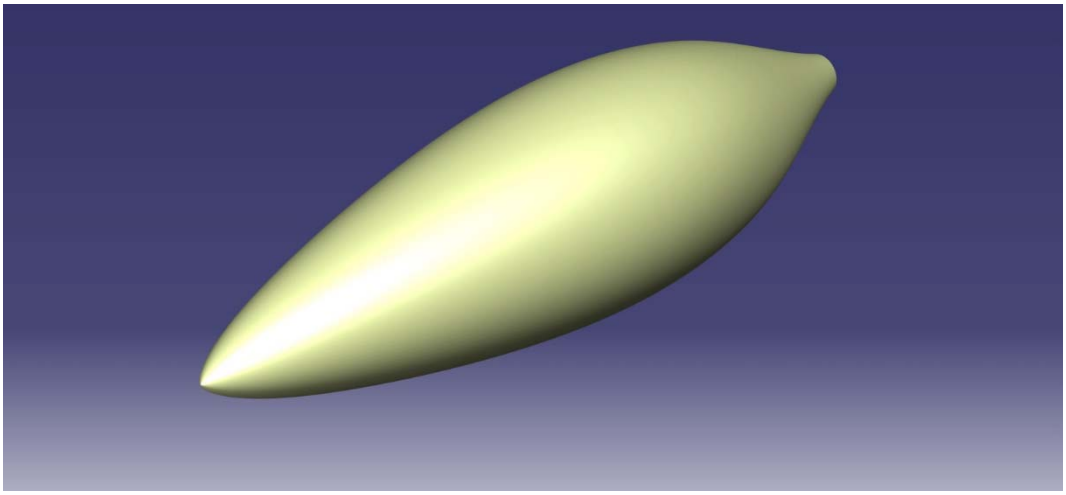

Figure 4.1 – Transformed airfoil body of revolution

4.1.1 CFD result

The results of the simulation for both the final vehicle body shape and its equivalent body of revolution (corresponding to the transformed airfoil body of revolution) can be observed on Table 4.1.

Table 4.1 - Vehicle comparison results

		AERO@UBI	Axisymmetric
Frontal Area	$A_{frontal}\ [m^2]$	0.3475	0.2785
Drag coefficient	$C_D\ [-X]$	0.0824211	0.0624877
Downforce coefficient	$-C_L\ [-Z]$	-0.208203	-0.0498332

As expected, the axisymmetric body has a lower drag. This is due to the fact that axisymmetric body has lower frontal and wetted area and it is a uniform streamlined body closer to the original airfoil geometry. The high value of downforce is caused by the bottom curvature in the middle of the final car body, near the center of gravity of the pilot (see Figure 3.12), which remembers an inverted airfoil. To improve this result the curvature given to the revolution body symmetry axis needs to be revised in the future development of the car, a change of the angle of attack or the vehicle or a change in the ground clearance height.

Regarding the drag value for the final vehicle AERO@UBI, an estimation of the final drag with the wheels and respective cavities was obtained using Hoerner [3] to complement the CFD simulation drag value. Hoerner explains that the drag caused by transverse gaps or cavities is a function of their width and depth. In Figure 4.2 it is represented the variation of the drag coefficient of transverse gap in function of e/h for frontal area equal to $h \cdot b$, where e is the length, b the width and h the depth of cavity. The value of the cavity drag coefficient will affect the drag coefficient of the vehicle by an increase shown on equation (4.1).

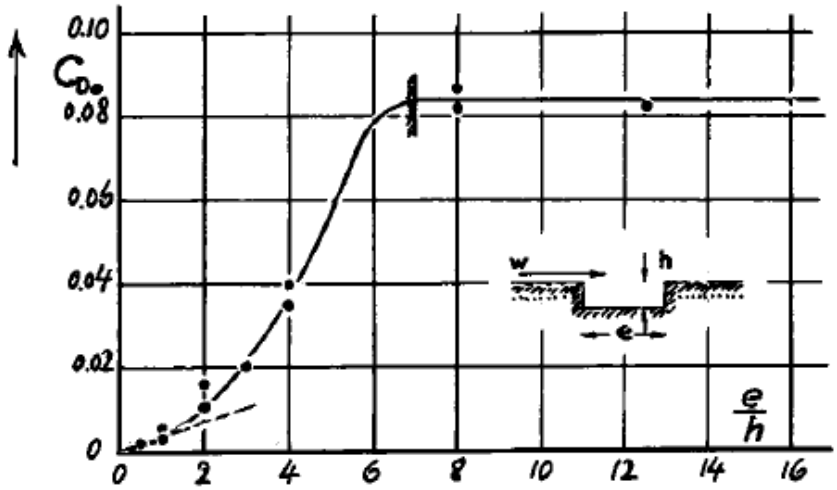

Figure 4.2 - Drag coefficient (on h times b) of transverse gaps [3].

$$C_D^* = C_D + C_{D_x} \cdot \frac{S_x}{S} \tag{4.1}$$

where,

C_D^* - Final drag coefficient of the body

C_D – Actual drag coefficient of the body

C_{D_x} – Drag coefficient of the component x

S_x – Frontal area of the component x

S – Frontal area of the vehicle

With CATIA it was possible to define the dimensions of the existent cavities of the vehicle, which are, one under the nose due to the front wheel, and two on the fairings (see Table 4.2).

Table 4.2 - Definition of cavities dimensions

	Two fairings	Nose Cavity
$e\ [m]$	0.5656	0.4465
$b\ [m]$	0.0968	0.1201
$h\ [m]$	0.2975	0.2156
e/h	1.90	2.03
$S_x\ [m^2]$	2 × 0.028798	0.026470

Through the analysis of Figure 4.2 and the cavities dimensions the C_D of the vehicle with the contribution of cavities is 0.085137.

Hoerner also explains that the drag coefficient of wheels can be based on the wheels frontal area, equal to tire width, b, times outer diameter,d (see Figure 4.3). In the present case the outer diameter is defined as the dimension of the apparent wheel. Here again with the use of CATIA it was defined the dimensions for the two rear wheels and the front wheel (see Table 4.3).

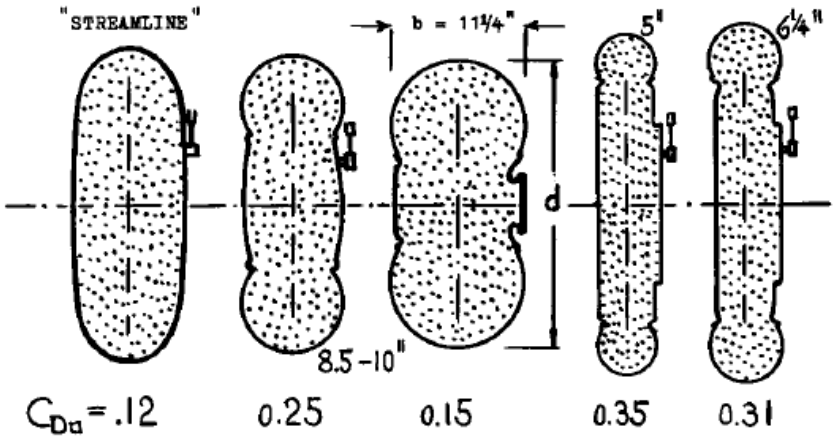

Figure 4.3 - Drag coefficient based on area b times d of wheels

Through the analysis of Figure 4.3 and the wheels dimensions the final C_D of the vehicle with the contribution of cavities and wheels is 0.0883348. The frontal area of the vehicle with the wheel is now $0.3522 m^2$.

Table 4.3 - Definition of wheels dimensions

	Two rear wheels	Front wheel
$b\ [m]$	0.044532	0.044532
$d\ [m]$	0.2305	0.2644
$S_x\ [m^2]$	2×0.010266	0.011773

To have a better perception if it is or not a good value for a SEM prototype vehicle, this value was compared with the main reference vehicles presented as state of the art in the literature review. As shown in Table 4.4 the values obtained by our vehicle are higher than the others SEM vehicles. The tall size of the pilot at the time of the present vehicle conception influenced decisively its aerodynamic performance. Nevertheless, AERO@UBI shows the smaller drag coefficient after the PAC CAR II.

Table 4.4 - SEM vehicles comparison

	AERO@UBI	Pac Car II	IDRApegasus	ARTEMIDe	Microjoule	Fancy Carol
$S\ [m^2]$	0.3522	0.2540	0.2580	0.2840	0.310	0.210
C_D	0.0883348	0.075	0.093	0.1	0.1	0.12
$S \cdot C_D\ [m^2]$	0.031108	0.01905	0.023994	0.0284	0.031	0.0252

4.1.2 Pressure Distribution Results

To study the design concept of aerodynamic similarity between the airfoil, its transformed 3D fuse shape and the final car equivalent shape, an analysis of the pressure coefficient distribution along the their longitudinal axis was made. The objective is to check if the pressure distribution keeps the same profile. For that, multiple sections were defined along the 3D bodies e and for each section, the average pressure coefficient was calculated.

Figure 4.4 shows that the axisymmetric body and AERO@UBI have pressure coefficient profile, which indicates that the equivalent body of revolution concept is valid. Remind this concept is that where the cross section area distribution is the same, the 3D bodies are aerodynamically equivalent. When compared with the airfoil the similarity is not reached but the trends are there. The leading edge of the airfoil has a higher pressure coefficient magnitude than the 3D bodies. That means that the vertical coordinate y of the airfoil should be transformed to a higher value to reach the same value of pressure coefficient. This increase of vertical coordinate can be translated on a bigger volume in the 3D body nose, to become available for the pilot's feet. The use of a fairing for the front wheel or a less sharpened nose. The same effect can be seen at the rear, where it is possible to have a more subtle cross section reduction towards the rear of the vehicle. The middle section of the vehicle has a higher absolute C_p value, this could be due to larger interference of the existence of the ground due to the rear

wheels fairings. To evaluate if the ground really affects this body region a simulation of the influence of the ground clearance on the pressure coefficient distribution was realized.

Figure 4.5 shows that the effect is higher when the vehicle is closer to the ground. This is due to the existence of fairings in this middle region that accentuates the Venturi effect, increasing the suction towards the ground. With this result it is possible to say that the fairings increase the absolute value of C_p and the downforce, which indicates that the fairings design needs to be reviewed. A possible solution is the use of a cambered airfoil with the upper surface positioned in the side of the car for the fairings design instead of a symmetric one.

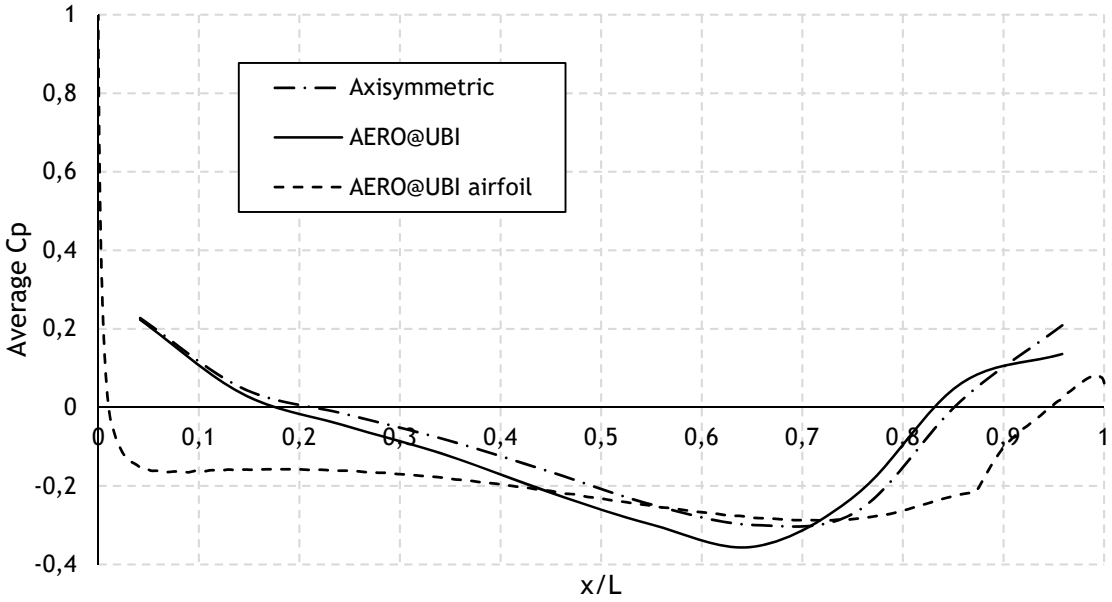

Figure 4.4 - Average Pressure Coefficient distribution

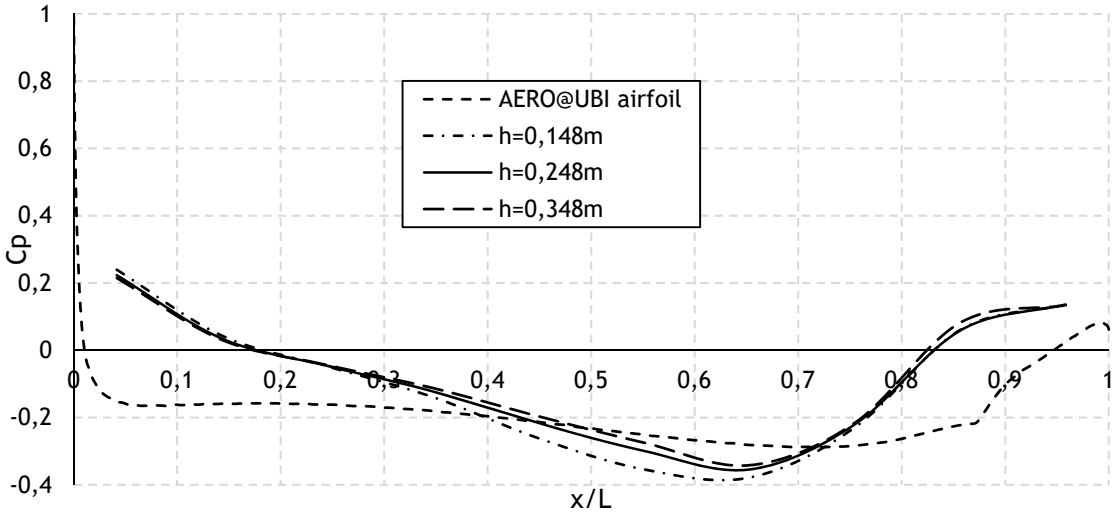

Figure 4.5 - Average Pressure Coefficient distribution for different ground clearance of AERO@UBI

4.1.3 Flow Separation Results

A brief analysis of the flow separation has been done to complement the pressure distribution analysis. To be possible to see the flow separation a scalar scene containing the wall shear stress along the x-axis can be seen in Figure 4.6 for the vehicle body and in Figure 4.7 for the axisymmetric body. Since the flow velocity is on the opposite direction of the X axis, and to have a better perception of the flow separation, only the positive values of shear stress are displayed, corresponding to the separated flow areas. It is seen that a small separation occurs at the rear of the vehicle and in the inner side the rear wheel fairings. The fairing separation was expected, since the angle between the direction of the incident flow and the tangent of the profile's rear end is too large, which causes an increase of adverse pressure gradient leading to a flow separation. In the case of the small rear separation zone, the high slope at the rear shape causes the same effect of the fairing, here it is possible to conclude that an exaggerated implementation of the equivalents areas can be prejudicial. This exaggeration is seen at the final section where this section is almost a 2D profile. The concept has to be applied in a smooth way to have a minimum flow separation.

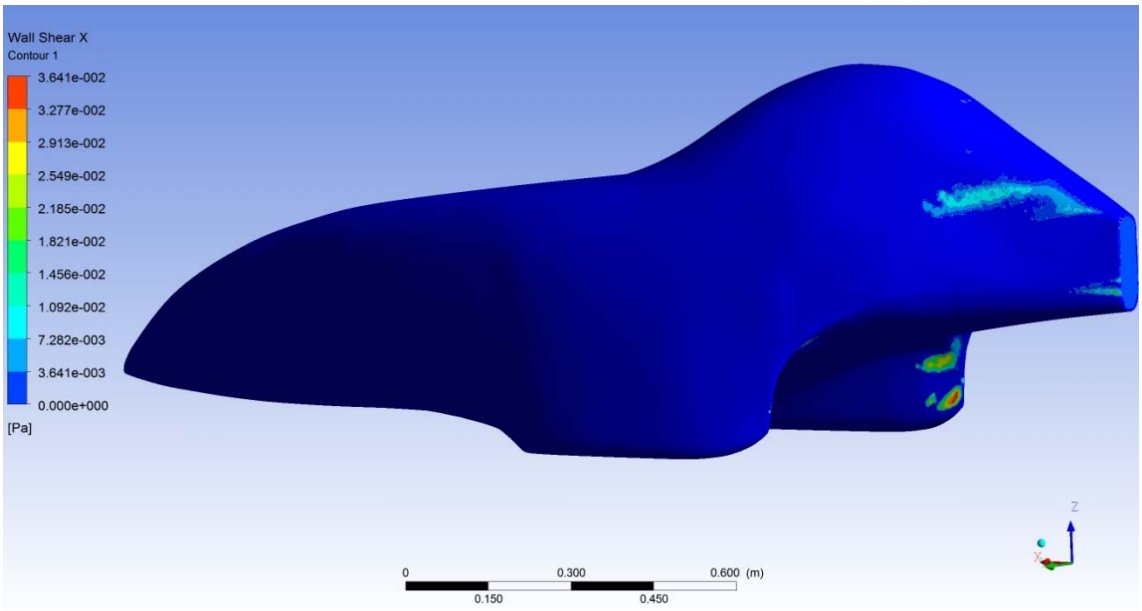

Figure 4.6 - Wall shear stress in x-direction of AERO@UBI showing small regions of separated flow in the final vehicle body design

On the axisymmetric body it is seen a separation only on the bottom body despite the fact of being a symmetric body. This separation is due to the existence of the ground. To verify the influence of the ground presence, a simulation of the axisymmetric body but with a symmetry condition for the ground was done.

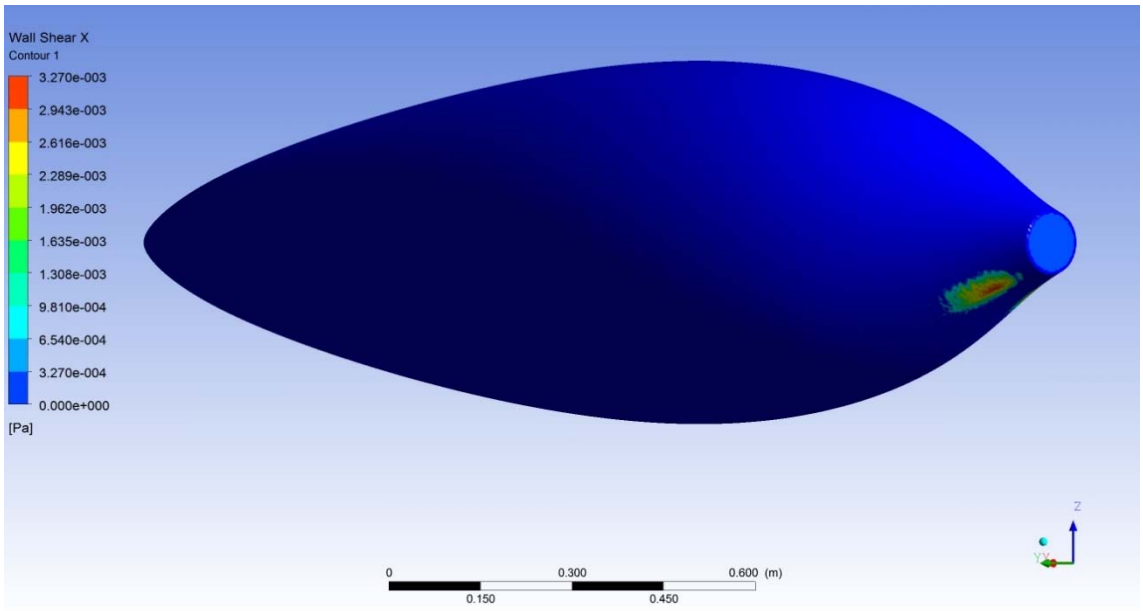

Figure 4.7 - Wall shear stress in x-direction of axisymmetric body showing small regions of separated flow in the vehicle body equivalent body of revolution

In Figure 4.8, the flow separation under the axisymmetric body disappears when the ground is no longer present, occurring only a separation at the end of the body which is normal due to the sudden tail cut of the shape. This result lead to run a simulation of the vehicle with the same boundary condition to see the influence on the result, it was also simulated with a moving wall condition for the ground to simulate the movement of the road under the vehicle.

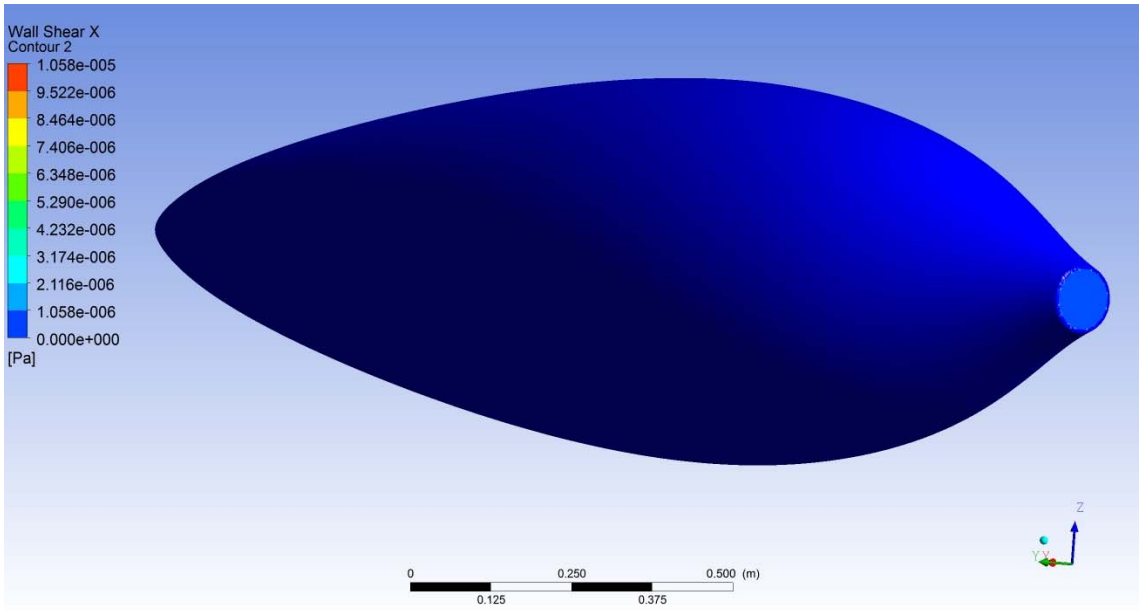

Figure 4.8 - Wall shear stress in x-direction of axisymmetric body with ground symmetry boundary

In Table 4.5 are shown the results for the drag coefficient value and downforce coefficient to different boundary conditions for the ground.

Table 4.5 - CFD results for different boundary conditions for the ground

	C_D	$-C_L$
Wall condition	0.082421	0.2082
Symmetry condition	0.080858	0.22641
Moving wall condition	0.080986	0.22683

The value of the drag decreases slightly, about 2% wit the moving wall condition. The same does not happen with the downforce, which suffers an increase of 8%. In the wall condition the velocity at the wall is 0, which means, that the velocity under the body will be lower since the wall will delay the flow. For the symmetry condition case the wall disappears, causing the velocity to be free of that constrain, thus reducing the pressure under the vehicle which causes an increase of the downforce. The same happens for the moving wall condition where the wall moves with the same velocity magnitude of the free stream flow. In terms of flow separation, the modification of the ground boundary conditions doesn't affected the localization of the separation regions on the 3D bodies.

4.2 Ground Clearance and Angle of Attack Influence

Since the values of downforce are higher than the desired absence of downforce, an analysis of the influence of ground clearance and angle of attack was performed to see if it is possible to reach a lower value of downforce, and consequently of the drag force.

4.2.1 Ground Clearance Influence

This simulation covers three distinct vehicle heights positions, with 10 cm of difference between them and the original position, being this a distance of 248 mm from the ground surface to the lowest underbody point. In Table 4.6 the obtained results are shown.

Table 4.6 - Ground Clearance influence results

Height [m]	h/L	C_D	$-C_L$
0.148	0.062	0.0906290	0.311312
0.248	0.103	0.0824198	0.208202
0.348	0.145	0.0798714	0.168417

As expected the values of downforce and drag force decrease when the ground clearance is higher, since the area behind the vehicle is higher, the ground effect is reduced. The downforce decreased approximately 19% and the drag about 3%. In fact, the maximization of the ground clearance was an implemented design concept since the beginning but the pilot view of the

road and the car height to wheel base maximum ratio limited the height to its original value 248 mm.

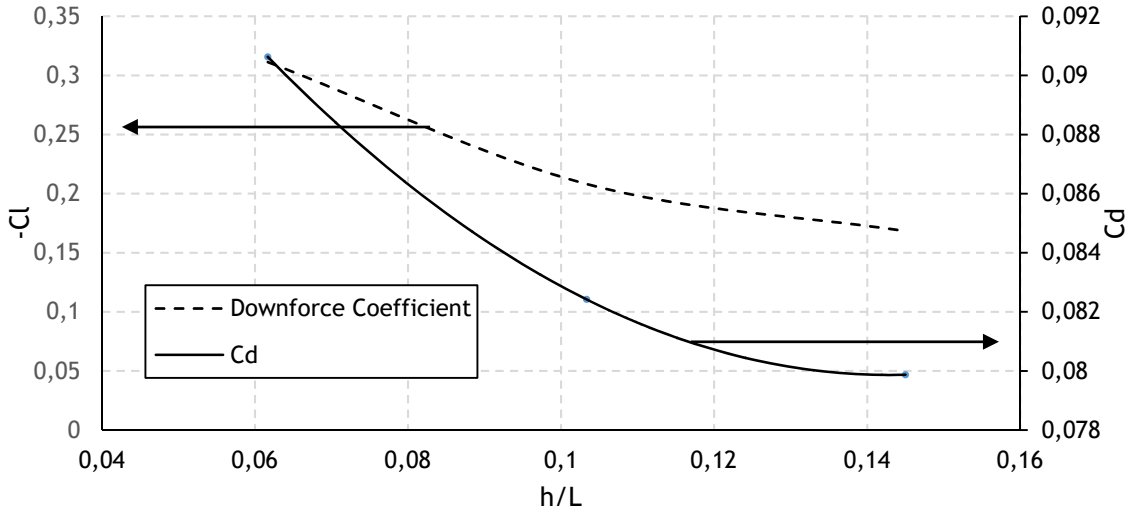

Figure 4.9 - Drag coefficient and Downforce coefficient variation with ground clearance

The graphic in Figure 4.9 shows the same behavior as the literature review (Figure 2.2), which confirms the theory with the present body shape, instead of a typical road vehicle bluff body.

4.2.2 Angle of Attack Influence

In this section a simulation of different setting of the vehicle's angle of attack was run. The center of rotation was set at the center of the front wheel, negative direction for angles of attack are defined in Figure 4.10.

Table 4.7 - Angle of Attack influence results

Angle of Attack α [°]	C_D	$-C_L$
2	0.086326	0,23668
0	0,08242	0,20820
-2	0,079772	0,18270
-5	0,079643	0,14179

In Table 4.7 it is seen that the values of downforce and drag force decrease when the angle of attack deacreses. This behaviour was expected since due to the geometry of the vehicle, when a negative angle of attack is applied the frontal area of the vehicle decreases too. The downforce deacrease a maximum of 31.8% and the drag a maximum of 3.3%, ie, the influence of the angle of attack has a higher impact on downforce than on the drag of the vehicle.

Nevertheless it is worthwhile to reduce the drag by minimizing the downforce of the vehicle. Only with CFD simulations like the present one the downforce can actually be minimized.

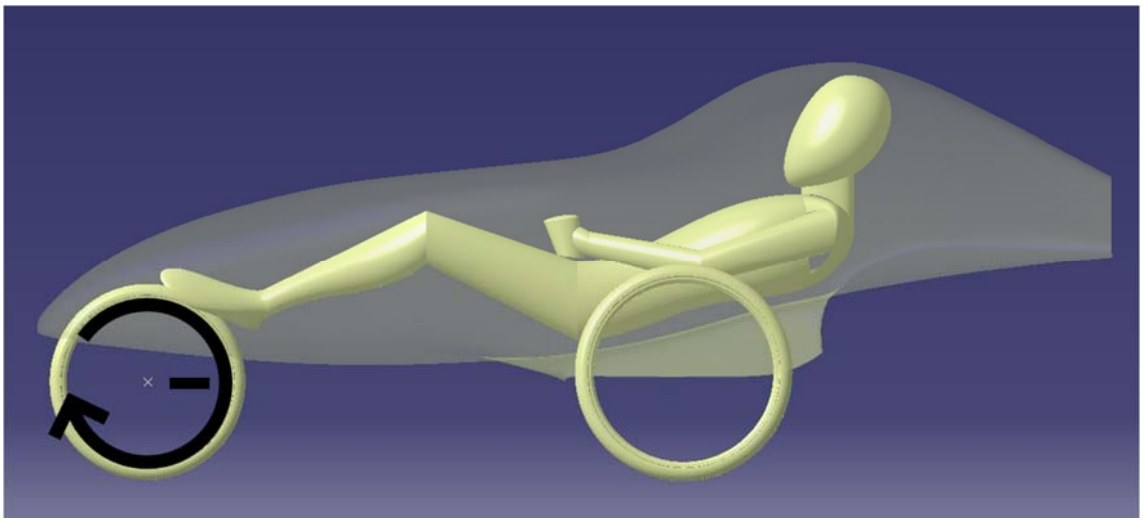

Figure 4.10 - Definition of negative angles direction.

The graphic in Figure 4.11 confirms the theory studied on literature review, since the C_L and C_D behaviors are similar with the Figure 2.5. As the ground clearance, the variation of angle of attack can be a good solution to reduce the effect of downforce.

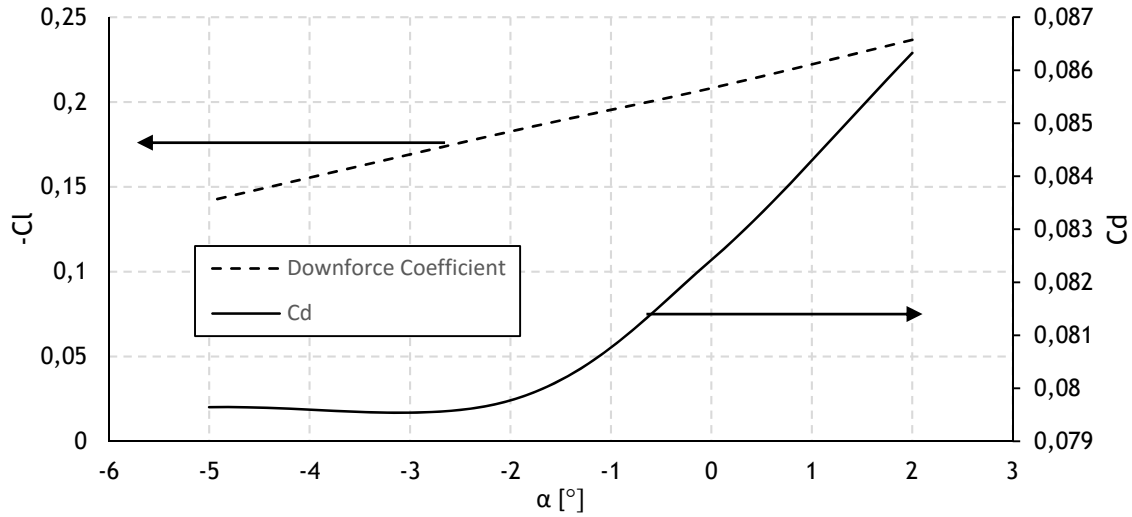

Figure 4.11 - Drag coefficient and Downforce coefficient variation with angle of attack

4.3 Exponential Value Influence

As explained on Chapter 3, Galvão [1] reached a first exponential value of 1.17 and made an approximation to 1.5. To observe the influence of the exponential value three axisymmetric bodies created with different values of exponentials: 1.17; 1.5 and 1.75 were simulated.

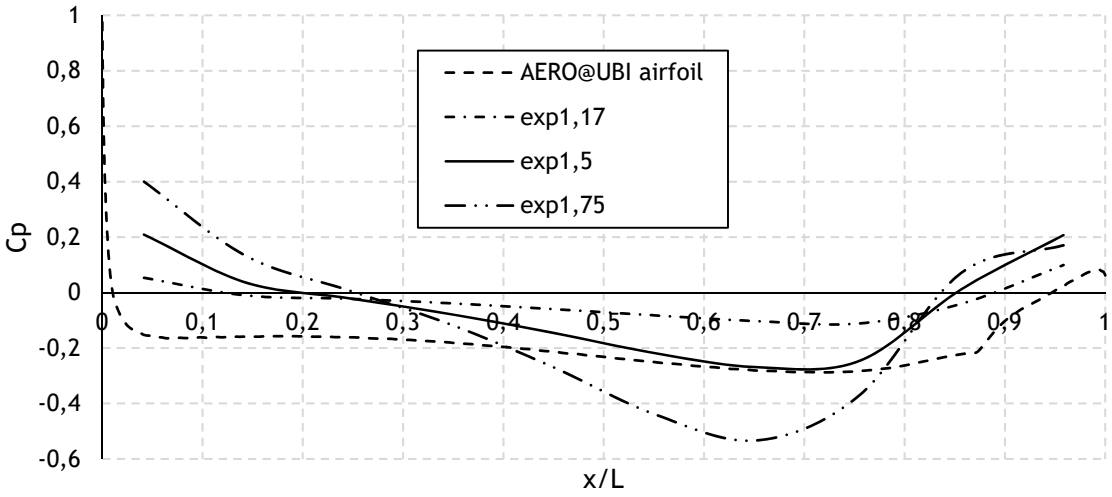

Figure 4.12 - Average coefficient pressure distribution for different exponential values

In Figure 4.12 is possible to observe that the approximation exponent of 1.17 initially proposed by Galvão is the one that corresponds to a better approximation of the original airfoil pressure distribution profile, despite showing a smaller pressure coefficient magnitude throughout the body length. However the resulting cross section area distribution of the 1.17 exponent airfoil transformation seems to need an expansion factor to reduce the slenderness of the transformed airfoil 3D body of revolution and thus reaching the same pressure coefficient magnitude.

5. Conclusion

A low-drag body is the key for a low energy consumption vehicle. With the present work it was possible the creation of a low-drag body based on innovative design concepts.

The first analysis of the present work shows that AERO@UBI is on the same aerodynamic baseline of other SEM prototype vehicles, but with an uncommon body shape.

The theory used to devise the design concepts was confirmed through comparison of the pressure coefficient distribution profiles of the 2D airfoil with that of the final vehicle.

The analysis of flow separation demonstrated that the vehicle has a low separated flow area on the rear and internal part of fairings near their trailing edges.

A larger nose volume and a smoother cross section area contraction vehicle tail, are the solutions proposed to achieve a better vehicle performance.

An analysis on the influence that the ground clearance and angle of attack have on the vehicle was performed. This analysis confirmed the general behavior reported by the existing literature.

Finally, a study on the influence of the exponential value of the airfoil transformation proposed by Galvão was accomplished. The fist approximation proposed by that author is accurate but a second thickening factor seems to be needed to obtain the same pressure coefficient in the 3D body as that of the original airfoil.

The present work resulted in several suggestions of possible modifications of AERO@UBI team SEM vehicle body design.

5.1 Future Works

To have a better perception of the vehicle's aerodynamic, a simulation with wheels and respective cavities can be realized in ANSYS Fluent. These additions on the geometry can reveal new separation zones and possibly a higher value of drag force, or different pressure coefficient distribution.

A new design of the vehicle can be realized with a lower frontal area, and with the implementation of the concept modifications that were suggested throughout the text.

In a new design it is necessary to take in account the camber to minimize the downforce.

The fairings design can be modified to reduce the flow separation appearing in the bottom of the vehicle and to have a better approximation to the airfoil C_p distribution.

Finally, due to the validation of this concept and the good results, a creation of a tool for auto adjustment of the cross section areas can be realized to have an easier concept implementation. Since the value of the y-coordinate can be higher in the nose of the vehicle, it is possible to study variations of vehicle noses to evaluate the influence in aerodynamics parameters and on the concept used.

A new design of the vehicle can be realized with a lower frontal area, and with the implementation of the concept modifications. Also it is necessary to take in account the camber to minimize the downforce. The fairings design can be modified to reduce the flow separation felted in the bottom vehicle and to have a better approximation to the airfoil C_p distribution.

Finally, due to the validation of this concept and the good results, a creation of a tool for auto areas adjustment can be realized to have an easier concept implementation.

References

[1] F. L. Galvão, "Nota técnica sobre corpos fuselados," São José dos Campos, 1968.

[2] "Fancy Carol : super mileage car team in Japan," [Online]. Available: http://www.fc-design.jp/fancycarol/index.htm. [Accessed 17 July 2015].

[3] S. F. Hoerner, Fluid-dynamic Drag: Practical Information on Aeodynamic Drag and Hydrodynamic Resistance, Sighard F. Hoerner, 1965.

[4] J. John David Anderson, Fundamentals of aerodynamics, 5th ed., McGraw-Hill, 2010.

[5] J. Katz, "Aerodynamics of Race Cars," *The Annual Review of Fluid Mechanics,* vol. 38, pp. 27-63, 2006.

[6] G. Tamai, The Leading Edge: Aerodynamic design of ultra-streamlined land vehicles., Robert Bentley, 1999.

[7] J. Katz, Race Car Aerodyamics: Designing for Speed, Bentley Publishers, 1995.

[8] H. K. Versteeg and W. Malalasekera, An introduction to computacional fluid dynamics: The finite volume method, Longman Scientific & Technical, 1995.

[9] P. Moin and K. Mahesh, "DIRECT NUMERICAL SIMULATION: A Tool in Turbulence Research," *Annual Review of Fluid Mechanics,* vol. 30, pp. 539-578, 1998.

[10] A. Fluent, ANSYS FLUENT Theory Guide 14.0, ANSYS Inc, 2011.

[11] M. Maciejewski and W. Osmólski, "Numerical Simulation Of The Blockage Effect In Wind-tunnels," in *Proceedings 14th European Simulation Symposium*, Dresden, Germany, 2002.

[12] C.-K. Choi and D.-K. Kwon, "Wind tunnel blockage effects on aerodynamic behavior of bluff body," *Wind and Structures,* vol. 1, pp. 351-364, 1998.

[13] J. B. Barlow, W. H. Rae and A. Pope, Low-Speed Wind Tunnel Testing, 3rd ed., John Wiley & Sons, Inc., 1999.

[14] H. Schlichting, Boundary Layer Theory (Translation in english of Grenzschicht-Theorie), 7 ed., United States of America: McGraw-Hill, Inc., 1979.

[15] F. Inc., Fluent 6.2 User's guide, January 2005.

[16] K. Sreenivasan, "The turbulent boundary layer," in *Frontiers in Experimental Fluid Mechanics*, Springer, 1989, pp. 159-209.

[17] W. L. Oberkampf, M. M. Sindir and A. T. Conlisk, Guide for the Verification and Validation of Computational Fluid Dynamics Simulations, AIAA, 1998.

[18] S. R. Ahmed, G. Ramm and G. Faltin, "Some Salient Features Of The Time-Averaged Ground Vehicle Wake," SAE Techinal Paper, 1984.

[19] J. J. Santin, J. Bernard, C. H. Onder, D. Isler, P. Kobler, F. Kolb, N. Weidmann and L. Guzzella, The World's Most Fuel Efficient Vehicle : Design and Development of Pac Car II, vdf Hochschulverlag AG, 2007.

[20] "ETH PAC-CAR II," [Online]. Available: http://www.paccar.ethz.ch/pictures/pac_car_II_miscellaneous.html. [Accessed 12 August 2015].

[21] informazione.it, "Premiata anche l'Italia alla Shell Eco-marathon Europe 2009," [Online]. Available: http://www.informazione.it/c/5F6B1BCF-86BB-4536-AB78-CE6C5019D817/Premiata-anche-l-Italia-alla-Shell-Eco-marathon-Europe-2009. [Accessed 13 September 2015].

[22] M. S. Carmeli, F. C. Dezza, G. Galmarini, M. Mauri and L. Piegari, "A vehicle with very low fuel consumption: realization, analysis and optimization," in *XIX Internacional Conference on Electrical Machines*, Rome, 2010.

[23] M. Carello and A. Messana, "IDRApegasus: a fuel-cell prototype for 3000 km/L," *Computer-Aided Design and Applications,* pp. 1-11, 2015.

[24] "Team H2politO," [Online]. Available: http://areeweb.polito.it/didattica/h2polito/veicoli/idra/idrapegasus.html. [Accessed 10 September 2015].

[25] "Champions of extreme fuel efficiency," SHELL GLOBAL, [Online]. Available: http://www.shell.com/global/environment-society/ecomarathon/events/europe/2014-highlights/microjoule-champions-of-extreme-fuel-efficiency.html. [Accessed 12 July 2015].

[26] "La Joliverie: 2 projects, 2 world records, 2 energies," [Online]. Available: http://en.calameo.com/read/001289329285c0ac4f826. [Accessed 12 July 2015].

[27] M. Copson, "Engineers of the future rev up at UK Eco-Marathon," *Shell Global Solutions Impact Magazine,* no. 1, p. 6, 2006.

[28] M. O.Kramer, "Hydrodynamics of the Dolphin," in *Advances in Hydroscience*, vol. 2, 1965, pp. 111-130.

[29] C. H. Gibbs-Smith, Sir George Cayley's Aeronautics, 1796-1855, London: Her Majesty's Stationery Office, 1962.

[30] H. Ashley and M. Landahl, Aerodynamics of wings and bodies, Courier Corporation, 1965.

[31] Shell Eco-marathon, Official Rules: Chapter 1, 2014.

[32] Shell Eco-marathon, Official Rules: Chapter 2, 2014.

[33] M. Drela, "XFOIL: An Analysis and Design System for Low Reynolds Number Airfoils," Springer Berlin Heidelberg, 1989, pp. 1-12.

[34] A. Deperrois, "XFLR5 Analysis of foils and wings operating at low Reynolds numbers," 28 February 2013. [Online]. Available: http://sourceforge.net/projects/xflr5/files/. [Accessed 17 August 2015].

[35] M. S. Selig, "Low Reynolds Number Airfoil Design Lecture Notes," in *NATO Research and Technology Organization, Applied Vehicle Technology Panel*, 2003.

[36] "UIUC Airfoil Coordinates Database," [Online]. Available: http://m-selig.ae.illinois.edu/ads/coord_database.html.

[37] M. Drela and H. Youngren, XFOIL 6.9 User Primer, Cambridge, MA: Department of Aeronautics and Astronautics, Massachusetts Institute of Technology, 2001.

[38] "Blender TM," [Online]. Available: https://www.blender.org/.

[39] "HELYX-OS," Engys, 2015. [Online]. Available: http://engys.com/products/helyx-os.

[40] C. J. Greenshields, OpenFOAM User Guide Version 2.4.0, OpenFOAM Foundation Ltd., 2015.

[41] A. Jackson, "A Comprehensive Tour of snappyHexMesh," in *7th OpenFOAM Workshop*, Darmstadt, 2012.

[42] D. Darmofal, "Structured vs. Unstructured Grids," in *Aerodynamics 16.100*, 2005.

[43] Pointwise, "Compute Grid Spacing for a Given Y+," [Online]. Available: http://www.pointwise.com/yplus/. [Accessed 20 April 2015].

[44] F. R. Menter, "Zonal Two Equation k-ω Turbulence Models for Aerodynamic Flows.," in *24th Fluid Dynamics Conference*, Orlando, Florida, 1993.

[45] J. E. Bardina, P. G. Huang and T. J. Coakley, "Turbulence modeling validation.," AIAA paper 2121, 1997.

[46] P. G. Huang, J. E. Bardina and T. J. Coakley, "Turbulence Modeling Validation, Teststing, and Development," Nasa Technical Memorandum, 1997.

[47] M. Keating, "Accelerating CFD Solutions," *ANSYS Advantage: Excellence in Engineering Simulation,* vol. V, no. 1, pp. 48-49, 2011.

[48] A. Bakker, "Lecture 5 - Solution Methods: Applied Computational Fluid Dynamics," in *Computational Fluid Dynamics (ENGS 150)*, Dartmouth College, 2002-2006.

[49] H. Lienhart, C. Stoots and S. Becker, "Flow and Turbulence Structures in the Wake of a Simplified Car (Ahmed Model)," in *New Results in Numerical and Experimental Fluid Mechanics III*, Springer Berlin Heidelberg, 2002, pp. 323-330.

[50] A. Fluent, ANSYS FLUENT User's Guide 15.0, Ansys Inc, 2013.

Appendix A

Table A.1 - Dimensions limits for prototype SEM vehicle [31]

Vehicle maximum height	$< 1000\ mm$
Vehicle track width	$\geq 500\ mm$
Ratio maximum height/track width	≤ 1.25
Vehicle wheelbase	$\geq 1000\ mm$
Maximum total vehicle width	$< 1300\ mm$
Maximum total length	$< 3500\ mm$
Maximum vehicle weight	$\leq 140\ kg \mid Driver$

Appendix B

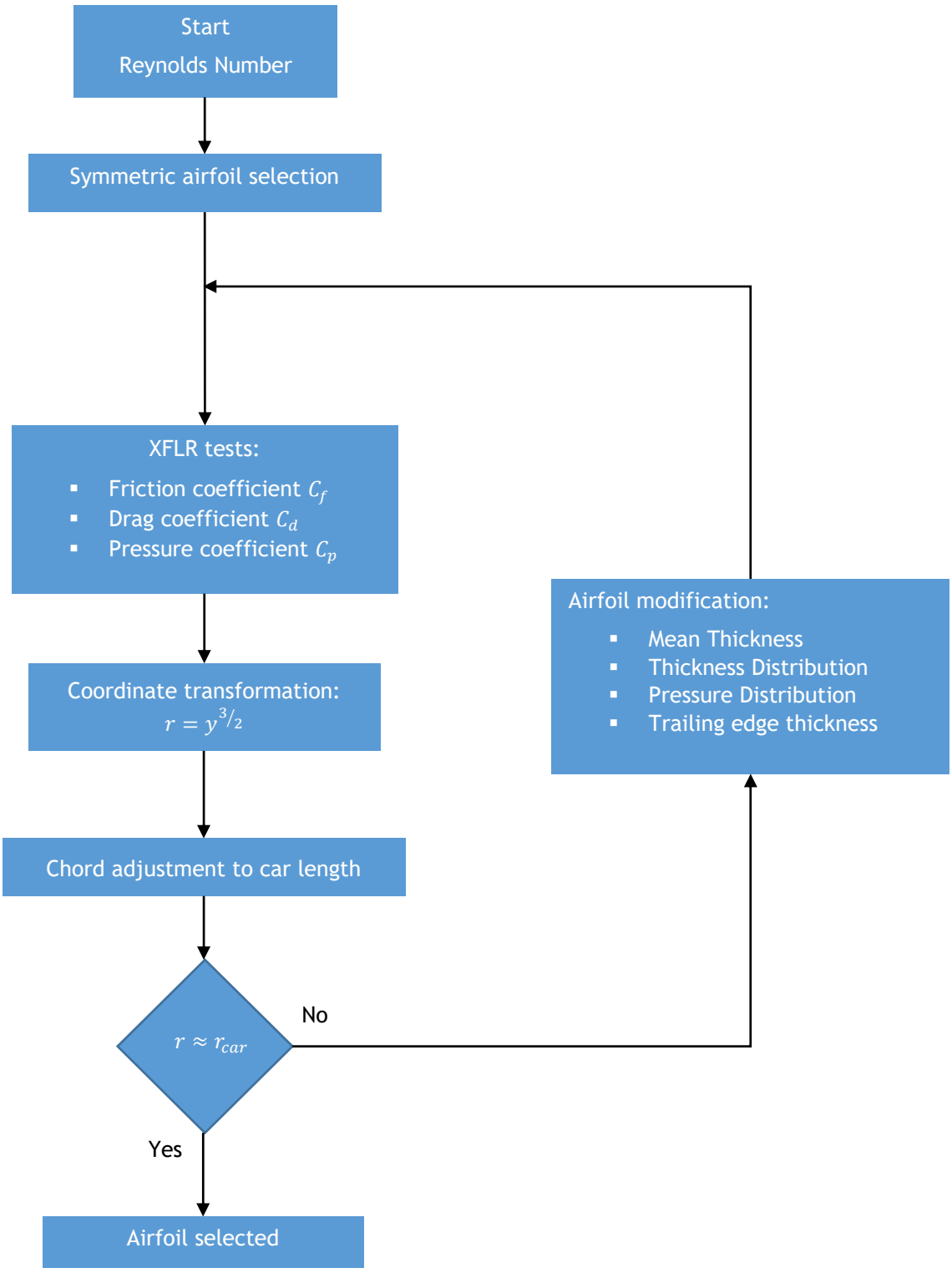

Figure B.1 - Airfoil selection flowchart